Humidity-Induced Degradation Processes of Halide Perovskites Unveiled by Correlative Analytical Electron Microscopy

Salim Mejaouri, Stefania Cacovich, Philippe Baranek, Baptiste Bérenguier, Iwan Zimmermann, Armelle Yaiche, Dominique Loisnard, Jean Rousset, Stéphane Collin

Humidity-induced degradation processes of halide perovskites unveiled by correlative analytical electron microscopy

Salim Mejaouri [1,2,5], Stefania Cacovich[3], Philippe Baranek [1,2], Baptiste Bérenguier [3], Iwan Zimmerman [2], Armelle Yaiche [1,2], Dominique Loisnard [4], Jean Rousset [1,2], Stéphane Collin[2,5]*

[1] EDF R&D, EDF Lab Paris-Saclay, Department SYSTEME, 7 boulevard Gaspard Monge, 91120 Palaiseau, France
[2] IPVF, Institut Photovoltaïque d'Ile-de-France, 18 Boulevard Thomas Gobert, 91120 Palaiseau, France
[3] Institut Photovoltaïque d'Île-de-France (IPVF), UMR 9006, CNRS, Ecole Polytechnique, IP Paris, Chimie Paristech, PSL, Palaiseau, 91120, France
[4] EDF R&D, EDF Lab Les Renardières, Department MMC, Avenue des Renardières, 77250 Écuelles, France
[5] C2N, Centre de Nanosciences et de Nanotechnologies, CNRS, Université Paris-Saclay, 10 boulevard Thomas Gobert, 91120 Palaiseau, France

Keywords: Hybrid perovskites, degradation, humidity, electron microscopy

Abstract

Improving the stability of lead halide perovskite solar cells (PSCs) for industrialization is currently a major challenge. It has been shown that moisture induces changes in global PSC performance, altering the nature of the absorber through phase transition or segregation. Understanding how the material evolves in a wet environment is crucial for optimizing device performance and stability. Here, the chemical and structural evolution of state-of-the-art hybrid perovskite thin-film $Cs_{0.05}(MA_{0.15}FA_{0.85})_{0.95}Pb(I_{0.84}\ Br_{0.16})_3$ (CsMAFA) is investigated after aging under controlled humidity with analytical characterization techniques. The analysis is performed at different scales through Photoluminescence (PL), X-ray Diffraction Spectroscopy (XRD), Cathodoluminescence (CL), Selected Area Electron Diffraction (SAED), and Energy Dispersive X-ray Spectroscopy (EDS). From the analysis of the degradation products from the perovskite layer and by the correlation of their optical and chemical properties at a microscopic level, different phases such as lead-iodide (PbI_2), inorganic mixed halide $CsPb(I_{0.9}Br_{0.1})_3$ and lead-rich $CsPb_2(I_{0.74}Br_{0.26})_5$ perovskite are evidenced. These phases demonstrate a high degree of crystallinity that induces unique geometrical shapes and drastically affects the optoelectronic properties of the thin film. By identifying the precise nature of these specific species, our multi-scale approach provides insights into the degradation mechanisms of hybrid perovskite materials, which can be used to improve PSC stability.

1. Introduction

In the past decade, perovskite materials have emerged in the field of semiconductors physics and in photovoltaics thanks to their excellent optical and transport properties, such as high absorption coefficient and long carrier lifetimes [1–3]. However, device stability and reliability under real operating conditions must be improved to enable commercialization [4–7]. One of the main factors affecting perovskite stability is humidity, especially when coupled with other environmental stresses such as light, air, or heat [4,6,8,9].

In terms of material stability, several reports have been published in the past years on perovskite degradation mechanisms [6,10–12], the reversible effect of light [13], the role of humidity in phase transition [14] or the actual aftermath of coupled stresses [15]. Specifically, a number of studies are focusing on the impact of moisture on hybrid perovskites and the processes that underlie degradation. The initial transformation mechanism has been found to lead to the formation of a hydrated (and di-hydrated) perovskite phase. This is a reversible process inducing a structural transformation usually revealed by crystallographic measurements [16–18]. Hybrid perovskite hydration then creates hexagonal polytypes as intermediate species when subjected to moist air [19]. Further exposure to water dramatically affects perovskite chemical composition. The formed hydrated phase then releases both organic cations and halides in a gaseous form [16,20–22]. This phenomenon stems from the interaction between perovskite constituents and water vapor. The underlying decomposition pathway is defined as a hydrogen bond that exists between organic cations formamidinium or methylammonium (FA^+ or MA^+) and water molecules. This bond breaks the octahedron $[PbX_6]^{4-}$ symmetry. Finally, the perovskite releases the halides as gaseous hydroiodic acid, HI (and HBr), and the cations as gaseous methylamine MA (and formamidine FA), while decomposition products containing the remaining elements start to appear. This mechanism has been reported for various perovskite compositions like MAPI[18,23,24], double-cation [16,19,25,26], and triple-cation [27,28] perovskite thin-film.

In the literature, there has been an increase of degradation studies on multi-cation mixed halide perovskites stability with spatially resolved spectroscopy techniques. Of particular note is the contribution of Doherty et al. [29,30] in the understanding of the origins of state-of-the-art perovskite degradation under environmental stress. Notably, when a specimen was exposed to light, degradation sites emerged where FA-rich regions showed octahedral tilting and hexagonal-phase impurities.

However, there are still several open questions regarding the identification of the different degradation products formed in humid environments. The aforementioned study by Doherty et al. uses state-of-the-art photoemission spectroscopy coupled with scanning electron microscopy techniques to reveal the degradation mechanisms of hybrid perovskite. It is also worth mentioning the work of Llacer et al. [31] in which they combine Kelvin probe force microscopy (FM-KPFM) with conductive atomic force microscopy (C-AFM) to reveal variations in the local surface potential of the perovskite film with its current response. Interestingly, the authors have also attempted to correlate surface states with stability under water vapour exposure. These studies demonstrate how correlative microscopy analysis can lead to a better understanding of the degradation phenomena occurring in hybrid perovskite materials. Here, we use electron microscopy to observe humidity-induced chemical and optical changes of $Cs_{0.05}(MA_{0.15}FA_{0.85})_{0.95}Pb(I_{0.84}Br_{0.16})_3$ (CsMAFA) thin films, revealing the formation of new phases which are often undetected in macroscopic analysis. The formation of such compounds drastically affects the optoelectronic properties of perovskite thin films, potentially leading to a reduction of the device lifespan. We investigate perovskite thin films exposed to humid air (under 85% RH) during 30 minutes to 6 hours, and we perform successive characterizations at different scales, including X-ray Diffraction Spectroscopy (XRD), spectrally-resolved Photoluminescence (PL) imaging, Energy Dispersive Spectroscopy (EDS), Cathodoluminescence (CL) and Selected Area Electron Diffraction (SAED). These experimental results are then compared with first-principle calculations using Density Functional Theory (DFT) of crystalline structures and their bandgap. In this way, we determine the structural, optical, chemical, and morphological properties of multi-cation perovskite degradation products, and we highlight the emergence of three inorganic decomposition phases: PbI_2, $CsPb(I_{0.9}Br_{0.1})_3$ and $CsPb_2(I_{0.74}Br_{0.26})_5$. Finally, we propose mechanisms based on ion migration, organic cation volatilization, and phase transition governing the degradation of CsMAFA under moisture. Our approach, based on a multi-scale characterization technique and correlative analysis, provides insights into the degradation of hybrid perovskite materials and should help the development of the stable thin films required for photovoltaics applications.

2. Structural characterization

The structure under investigation includes the following layers: glass/FTO/SnO_2/perovskite, as shown in **Figure 1(a)**. The stack is exposed to humid air, with a level of 85% of relative humidity (RH) for different durations: 30 minutes, one hour, two, four, six and eight hours.

After 30 minutes the morphology of the perovskite evolves. In the optical image of **Figure 1(b)**, we note the emergence of several degradation products with unique geometries. As aging time increases, their density increases together with the formation of voids in the perovskite film (see **Figure S1(a)**).

The morphology of these new phases is further investigated by SEM imaging (**Figure S1(b)**). In the pristine thin film, we can easily identify the grain boundaries of the perovskite as well as the presence of PbI_2 clusters, due to the excess of PbI_2 in the precursor solution (see the Experimental section for details on the fabrication of the film). The average grain size is around 320 nm, in line with values reported for state-of-the-art PSC [32]. However, the humidity induced the formation of new compounds with four different morphologies: hexagonal, disc-like, flower-like, and needle-likes structures.

The decomposition of a perovskite film under humid air and the appearance of such features are consistent with previous reports [19,25,33]. Needle-like structures, for instance, were evidenced by Marchezi et al. in the study of the moisture effect on double-cation perovskite [19] and were related to hydrated perovskite intermediates. Similar observations were made in the investigation of the degradation mechanisms of $MAPbI_3$ [34]. Nishida et al. also report the emergence of needle-like heterogeneities in CsMAFA perovskite film exposed to water-vapor[33]. However, localized investigations of the composition and the structure of these degradation products is lacking in these studies, which prevented the identification of their specific nature.

We then performed XRD measurements with the whole series of diffraction patterns at different humidity exposure times reported in **Figure S1(c)**. **Figure 1(c)** shows the patterns obtained before and after 1 hour of aging when the main changes occur. We observe diffraction peaks at 14.09°, 31.8°, 34.9°, and 37.8° corresponding to (110), (310), (312), and (204) crystallographic planes of the CsMAFA tetragonal structure, respectively, confirming the initial state of the film. Additional Bragg peaks are present in the pristine thin film at 12.6°, and 38.7° and correspond to (001) and (003) planes of the hexagonal PbI_2. These peaks are usually observed when an excess of PbI_2 is introduced into the precursor solution [35]. In the XRD patterns of the aged samples, the PbI_2 contribution becomes more prominent. Besides, additional peaks appear at 11.2° and 32.9° that can be assigned to the (002) and (006) planes of inorganic $CsPb_2X_5$ tetragonal structure (where X stands for a halide) [36,37], suggesting the emergence of a full inorganic compound in the aged perovskite film.

Figure 1(d) displays the evolution with time of the area ratio of the most intense diffraction peaks of PbI_2 ($2\theta = 12.6°$) and $CsPb_2X_5$ ($2\theta = 11.2°$) over the CsMAFA main peak ($2\theta = 14.09°$)

when the samples are exposed to humid air (85 % RH) during up to 6 hours. The decrease of the CsMAFA peak intensity is counterbalanced by the emergence of PbI_2. It shows that perovskite decomposes into PbI_2 when exposed to moist air, as expected from previous studies [4,16,38]. In parallel, the CsMAFA/$CsPb_2X_5$ ratio also drops, which indicates a transformation of CsMAFA into $CsPb_2X_5$. This assumption is supported by the several works that have reported a similar water-induced phase transition in mixed-cation perovskites film [27,39]. After 4 hours of aging, the ratio CsMAFA/PbI_2 increases due to a decrease in PbI_2 content known to decompose into lead salts in humid air[40].

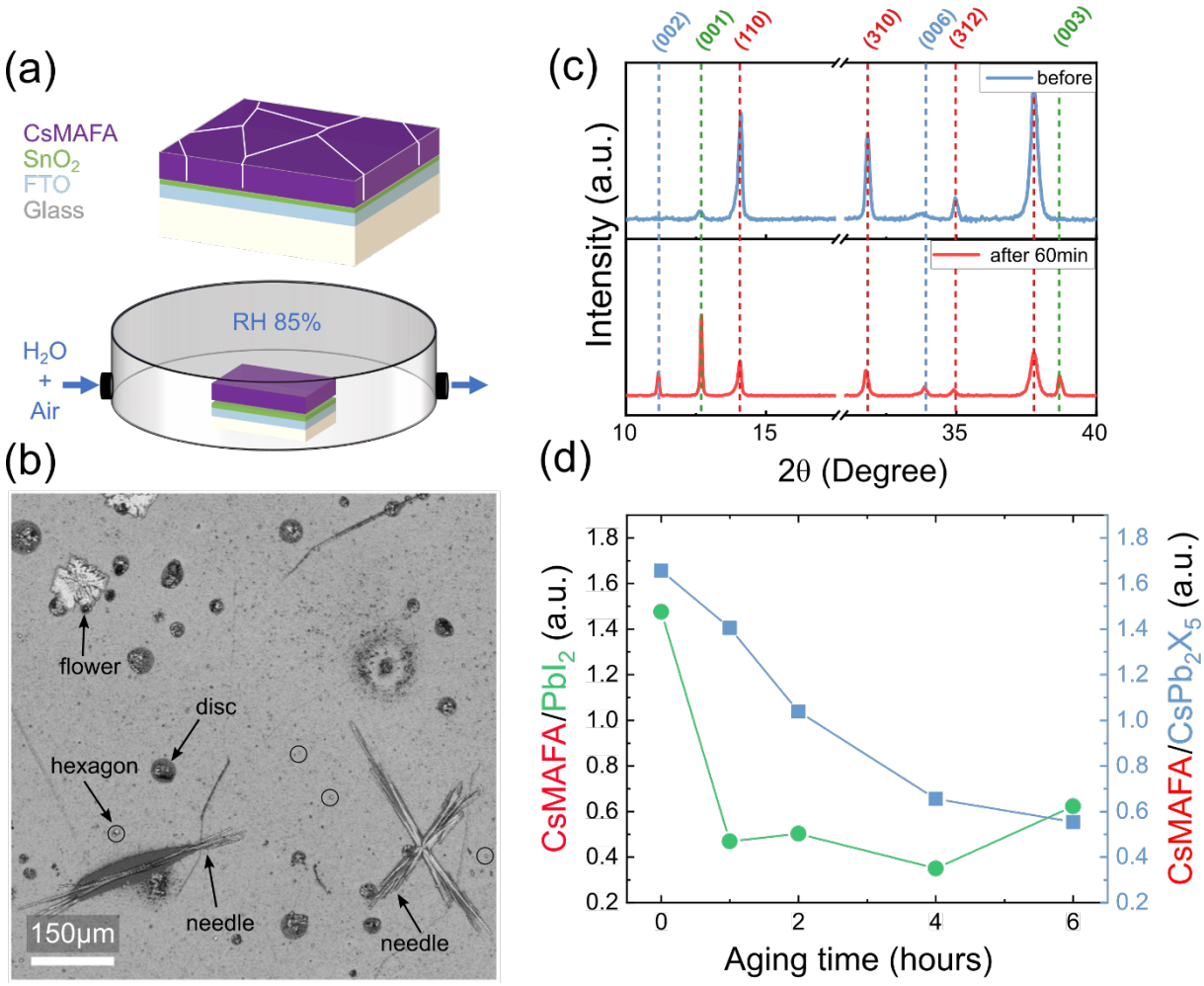

Figure 1 a) Sketch of a half-cell perovskite solar cell and of the climatic chamber. b) Optical microscope image of a CsMAFA film after exposure to 85% RH for 30 minutes. Various degradations features are highlighted: hexagon, flower, needle, and disc. c) Diffractograms obtained via XRD measurements performed before and after aging. XRD peaks of CsMAFA, PbI_2, $CsPb_2X_5$ are indexed in red, green, and blue, respectively, according to the study by Kazemi et al.[28]. d) Variation of the area ratio of the (110) CsMAFA peak over the (001) PbI_2 and (002) $CsPb_2X_5$ peaks, with aging time.

3. Photoluminescence Imaging

The formation of new phases in the perovskite layer could affect the optoelectronic properties of the absorber and therefore the device performance. To investigate this aspect, we performed photoluminescence (PL) imaging measurements [41]. We acquired maps for samples exposed to humidity for one, two, and four hours, locally monitoring the evolution of the PL spectra.

Figure 2(a) shows spatially averaged PL spectra for the four aging durations. Initially, the spectrum exhibits a maximum PL peak position at 1.61eV, that then progressively red shifts until reaching a value of 1.59eV after 4 hours. Moreover, the PL peak intensity significantly rises for increasing exposure times. Such moisture-induced evolution of the PL spectra of halide perovskite thin films was already observed in the literature [17,42] , and the increase of PL peak intensity was found to be proportional to the RH%.[16]

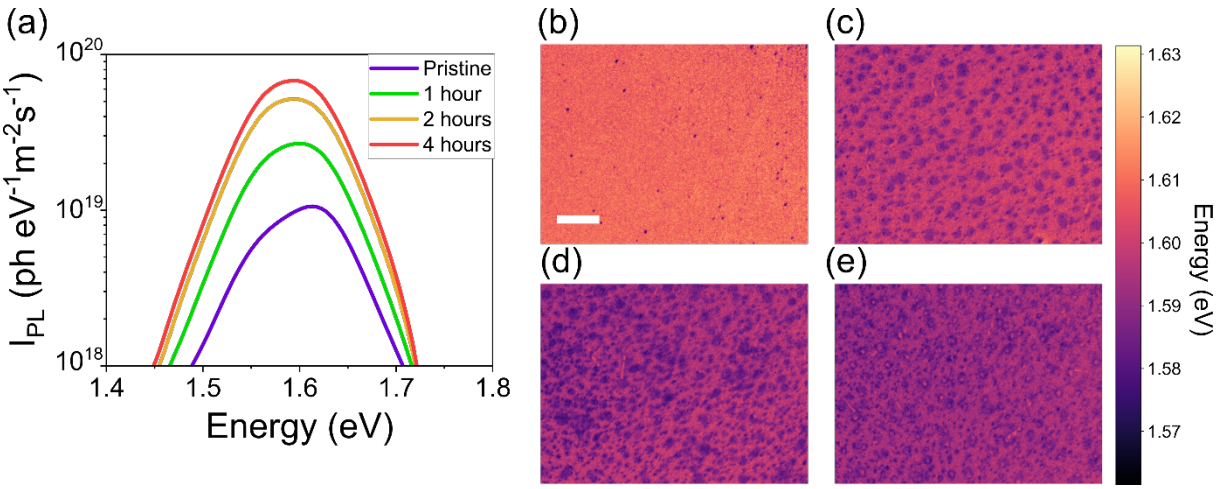

Figure 2. a) Spatially averaged (over an area of 700 x 950µm) photoluminescence spectra acquired on specimens exposed for 0, 1, 2, and 4 hours to an atmosphere with a level of 85% RH. Maps of the PL peak maximum position for **b)** pristine samples and samples aged for **c)** one hour, **d)** two hours, and **e)** four hours. The scalebar of 150 µm applies to all images.

A phenomenon widely reported in the literature is the segregation of the mixed halide perovskite into I-rich and Br-rich regions due to light exposure. This effect called the "Hoke effect", comes with a red shift of the overall PL emission peak. [43] In a recent study, Caprioglio et al. have shown that radiative transitions are facilitated in I-rich domains, which explains the increase in PL intensity.[44] Consequently, our observations can be related to halide segregation induced by moist air coupled with the effect of light as one map acquisition lasts approximately 10 minutes. We then examine the local distribution of the optical properties. In **Figure S2**, we

plot panchromatic PL maps for each specimen with the same intensity scale. We observe the apparition of highly luminescent features on the specimen aged for 1 hour and an overall increase of the PL signal intensity. Corresponding PL peak maximum position maps are displayed in **Figure 2(b-e)**. While the pristine sample (**Figure 2(b)**) shows a homogeneous distribution of the PL peak position at approximately 1.61 eV, the samples exposed to humid air exhibit a second phase emitting at 1.59 eV.

Spatially resolved investigation of the perovskite thin films thus reveals variations of their optoelectronic properties after aging. The PL peak intensity increase indicates a reduction of non-radiative losses, which might be related to the passivation of the surface defects of the perovskite layer [45] by humid air and to the formation of high emitting iodine –rich domains. However, some of the degradation products observed by optical microscope and detected by XRD measurements are not resolved by photoluminescence imaging.

This probably arises from their poor contribution to the overall active layer emission and to the fact that their size is of the order of micrometers thus not observable with the optical set-up used for the photoluminescence analysis. Although there is an increase of PL intensity and therefore a possible reduction of non-radiative losses, there is an increase of inhomogeneities in the thin films. These early signs of degradation expand for longer exposure times, leading to a general worsening of the absorber properties.

4. Correlative multi-modal electron microscopy analysis

In order to gain further insight into the humidity-induced degradation products, we performed a systematic nanoscale analysis by coupling several electron microscopy techniques. **Figure 3(a), (b),** and **(c)** show the SEM image and the elemental maps obtained via an SEM-EDS measurement on a hexagonal feature. Bromine (Br) and iodine (I) contents appear in red and green, respectively, allowing for a qualitative examination of the element distribution in this specific region. The hexagon exhibits higher I and lower Br contents than the surrounding film. Concentrations in Cs, Br, I, and Pb are estimated by element quantification (see Experimental Section for details) in the hexagon and in the surrounding film. The results are normalized by the concentration of Pb and are displayed in **Table 1**.

Table 1 – Results of the quantification of the composition in Cs, I, Br and Pb obtained via SEM-EDS measurements on a pristine CsMAFA film, and on the hexagon displayed in **Figure 3(a).**

Feature	I/Pb	Br/Pb	Cs/Pb	Composition
Film	2.6±0.3	0.5±0.1	0.07±0.02	CsMAFA
Hexagon	2.2±0.2	0.1±0.05	0	PbI_2

In the hexagonal feature, the I/Pb ratio is close to 2, indicating the formation of pure PbI_2. The presence of a small Br concentration (Br/Pb ≈ 0.1) may come from perovskite residues beneath the hexagon.

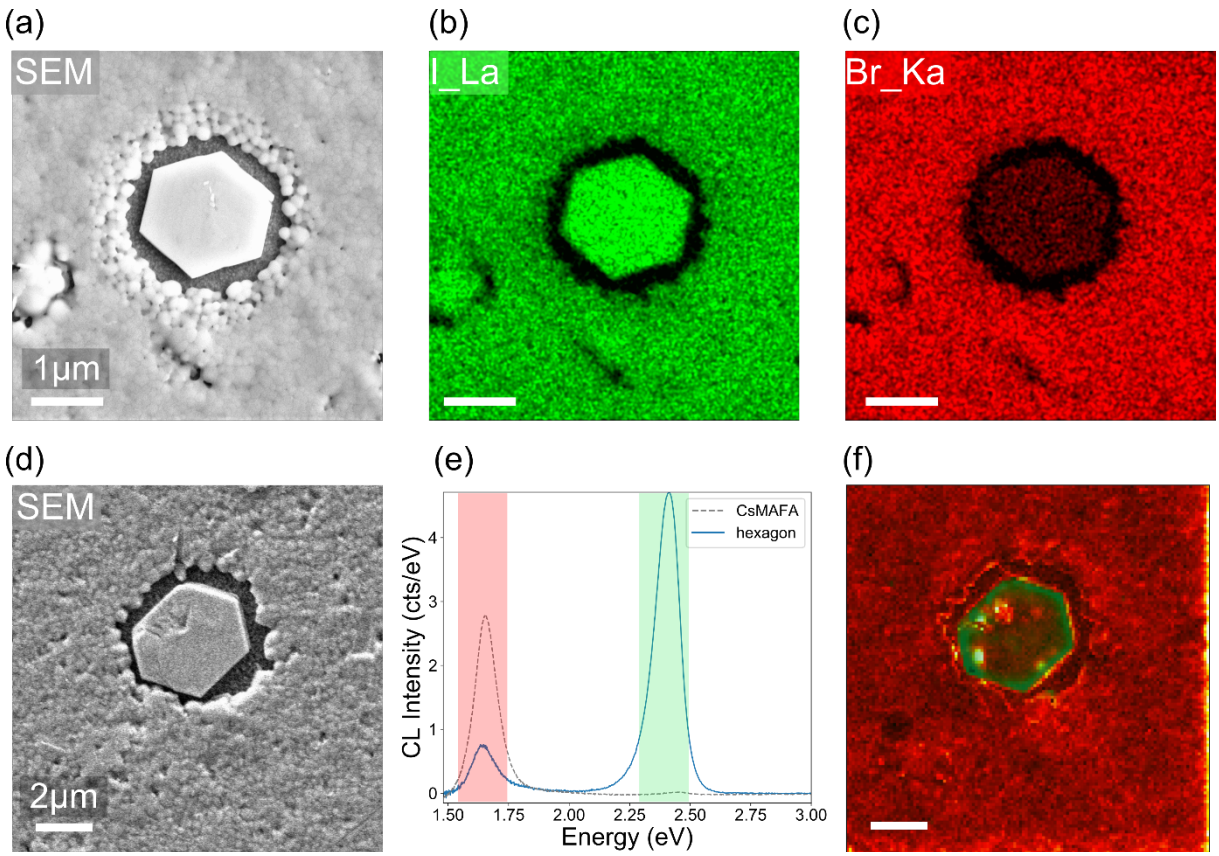

Figure 3. Hexagon feature. a) SEM image of the hexagon analyzed with EDS. b) and c) Corresponding EDS elemental maps showing the distribution of iodine and bromine in green and red, respectively. d) SEM image of the hexagon analyzed with CL. e) Averaged CL spectra integrated over the hexagon in blue and over a pristine CsMAFA perovskite film in gray (dash line). f) CL map with false colors showing the luminescence integrated over two different spectra regions: red [1.6eV, 1.7eV], and green [2.25eV, 2.5eV] corresponding to the emission of the CsMAFA perovskite and the PbI_2 phase, respectively. For each pixel, the integrated intensity of each band is normalized by the intensity integrated over the full spectral range.

This degradation product exhibits the typical hexagonal morphology of PbI_2 crystals, suggesting a highly anisotropic growth along the (001) axis. SEM images with a wide field-of-view show that most of the PbI_2 crystals resulting from perovskite decomposition have the same orientation (see **Figure S3**), in accordance with the steep increases of the PbI_2 contribution in XRD spectra shown in **Figure 1(c)**.

Hexagonal degradation products have been further characterized by CL, see **Figure 3(e,f)**. Their emission spectrum is compared to the pristine material (CsMAFA) and exhibits two visible peaks; the first one at 1.65eV is related to CsMAFA, and the other at 2.41eV is attributed

to the PbI_2 phase. This is confirmed by the CL maps plotted in **Figure 3(e)**, where the CsMAFA and PbI_2 peaks are highlighted in red and green, respectively. A weak but noticeable response around 1.65eV in the hexagon can be associated with remnants from the parent perovskite film located beneath the hexagon.

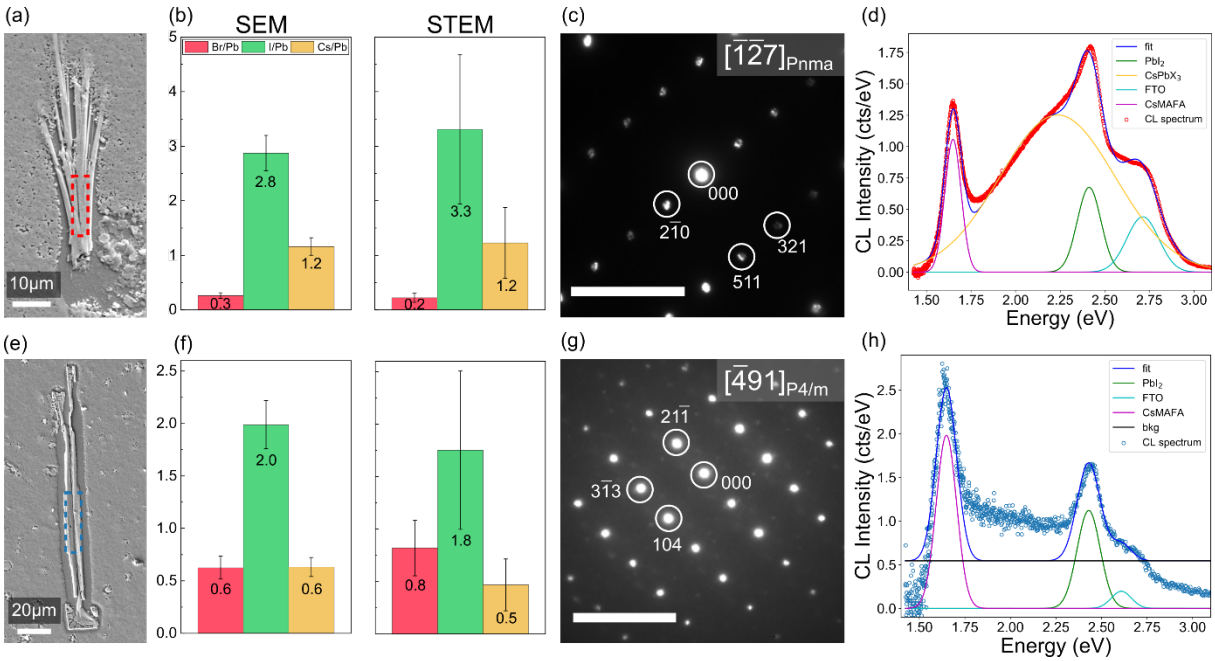

Figure 4. Correlative analysis of the needles displayed in **Figure S1(b)4-5**. (a,e) SEM images of the two needles studied. (b,f) Corresponding ratios of I/Pb, Br/Pb and Cs/Pb determined by quantification of SEM-EDS and STEM-EDS measurements, presented in a bar plot. Composition of needle (a) and (e) is equal to: $CsPb(I_{0.9}Br_{0.1})_3$ and $CsPb_2(I_{0.7}Br_{0.3})_5$, respectively. (c,g) Diffractogram obtained via Selected-area electron diffraction (SAED) measurements performed on the same type of needles as the one displayed in (a) and (e) (see **Figure S5**). Indexation shows that needle $CsPb(I_{0.9}Br_{0.1})_3$ diffraction pattern is oriented along the [$\underline{1}27$] zone axis and $CsPb_2(I_{0.7}Br_{0.3})_5$ along the [$\underline{4}91$] zone axis. The diffraction patterns fitted with simulated crystal structures are displayed in **Figure S6.A and B**. (d-h) Spatially averaged CL spectra in the needle presented in (a) and (e). CL spectrum (d) is fitted with 4 Gaussian functions corresponding to CsMAFA (in purple), $CsPb(I_{0.9}Br_{0.1})_3$ (in yellow), PbI_2 (in green), and FTO (in blue) contributions at 1.65, 2.25, 2.41, and 2.71 eV, respectively. CL spectrum (h) is fitted with 3 Gaussian functions corresponding to CsMAFA (in purple), FTO (in blue), PbI_2 (in green) contributions at 1.68, 2.41, and 2.71 eV, respectively. The background noise "bkg" is plotted in black.

Different needle-like structures can be found in the aged samples that do not differentiate by their morphology but present very distinct structural and optoelectronic attributes. We showed in **Figure S1(b)(4)** and **(5)** an example for each type of needle on which SEM-EDS, STEM-EDS, SAED, and CL are performed and presented in **Figure 4**.

I, Br, Cs, and Pb distribution maps obtained by SEM-EDS for each needle are displayed in **Figure S4**. Notably, the Cs and I content are higher in needles than in the surrounding remnant perovskite film. The quantification of the elements from SEM-EDS evidences that needles have a distinct composition. In the first needle (see **Figure 4(b)**), the ratio Cs/Pb is close to one suggesting the formation of a fully inorganic perovskite, i.e., $CsPbX_3$. In the second needle (see **Figure 4(f)**), on the other hand, the ratio Cs/Pb is close to 0.5, that could correspond to the lead-rich pure inorganic perovskite$CsPb_2X_5$.

Halogens' concentration also varies between the two specimens. In the second needle, the ratio I/Pb is systematically lower than in the first needle ($2 < 2.8$), while the ratio Br/Pb is slightly higher ($0.7 < 0.3$). We then propose the following composition for these cesium-based perovskites: $CsPb(I_{0.9}Br_{0.1})_3$ and $CsPb_2(I_{0.7}Br_{0.3})_5$. Given the limits of SEM-EDS for analyzing complex systems mixing low and high atomic number elements, the relevance of these compositions might be challenged. Therefore, FIB lamellae were prepared from the same type of needles and analyzed by STEM-EDS (see **Figure S5** for details). Results from quantification are displayed in the bar plots in **Figure 4(b)** and **(f)**. Although there are larger uncertainties due to the small volume probed (and thus fewer X-ray counts collected [46]), the results are similar to the SEM-EDS quantification, which supports the assumed composition of needles.

According to the literature, $CsPbI_3$ and $CsPbBr_3$ crystallize in various possible configurations depending on the temperature. The iodine-based compound is cubic at high temperature (above 310°C) and turns into ordered and disordered orthorhombic successively when temperature decreases. Its bromine-based counterpart goes from cubic (above 130°C) to tetragonal and then to orthorhombic phase[47].

The amount of this specific phase in the degraded film might not be high enough to be yielded in XRD measurements, which might explain why it is not present in the diffraction patterns around $2\theta = 10°$ or 15° as expected from such orthorhombic or cubic structures [48]. To determine the crystallographic nature of the $CsPb(I_{0.9}Br_{0.1})_3$, we performed SAED in a TEM on the same lamellae prepared by FIB milling (**Figure S5(a)**). The resulting diffraction pattern is displayed in **Figure 4(d)**. The presence of spots instead of rings suggests that the sample is composed of one monocrystal. These spots correspond to reflections of the impinging electrons with the lattice planes. To properly identify the crystallographic nature of the specimen, the

$CsPb(I_{0.9}Br_{0.1})_3$ structures cubic, ordered and disordered orthorhombic, triclinic and, tetragonal phases were simulated by DFT calculations. **Table 2** summarizes for each structure simulated the space group and the lattice parameters considered. Given the uncertainty on lattice parameters determined by electron diffraction patterns we assume that these parameters are correct for our specimens [49,50]. For each structure the bandgap is also calculated and indicated in **Table 2**.

These structures were then used to simulate electrons diffraction patterns in multiple crystalline orientations to fit the experimental diffraction pattern. **Figure S6.A** shows the results obtained overlayed with the experimental diffraction pattern. The deviation between the simulations and the experiment, expressed as the 'sum-of-square error' (Σs^2 in mm^2), is displayed in **Table S1**. The best fit (with the lowest Σs^2value) is obtained with the cubic structure ($Pm\underline{3}m$), yet diffraction patterns of the ordered and disordered orthorhombic structures also matching well the experimental pattern. SAED is a technique that can produce similar diffraction patterns for distinct crystalline structures and orientations [46]. Hence, the accurate discrimination between the presumed symmetries of $CsPb(I_{0.9}Br_{0.1})_3$ would require complementary structural measurements or an additional calibration of the SAED measurement.

To investigate its optoelectronic properties, we performed CL on the same needle $CsPb(I_{0.9}Br_{0.1})_3$ specimen at room temperature. **Figure 4(d)** presents the spatially averaged (in the red-dashed square in **Figure 4(a)**) CL signal where four optical transitions are present: a peak at 1.65eV assigned to the remaining perovskite phase, one at 2.41eV corresponding to PbI_2 emission, and finally, two peaks at 2.71 and 2.25eV. We use four Gaussian functions to decompose the spectrum (see **Table S2** for fitting parameters).

To localize the source of these emissions we integrate the luminescence on the following spectral ranges: 2.71±0.09eV, 2.23±0.06eV, 2.41±0.05eV, and 1.6±0.01eV. The integrated luminescence is normalized on each pixel by the integrated luminescence over the full spectral range (from 1.5 to 3eV) and the obtained filtered CL maps are plotted in **Figure S7(a)**. The needle is emitting luminescence in the two first filtered CL maps, suggesting that the two peaks at 2.71 and 2.25eV in the spectrum may be attributed to the $CsPb(I_{0.9}Br_{0.1})_3$ phase. However, the first filtered map shows that the FTO layer beneath the needle also emits in this spectral range (blue arrow). The CL peak at 2.17eV may thus originate from both the needle and the FTO.

The PbI_2 hexagons present in the bottom-right corner of the map are emitting in the second filtered CL map due to the broadness of their CL peak localized at 2.41eV. Small clusters are emitting in the needle in the third filtered CL map.

Table 2 lists the calculated values of the bandgap of $CsPb(I_{0.9}Br_{0.1})_3$ perovskite according to the different crystallographic structures. The cubic $CsPbI_3$ and $CsPbBr_3$ are also added for comparison purposes. Given the high injection condition in CL acquisitions, previous studies have considered that CL peak position corresponds to the bandgap of the material analyzed [44]. We therefore venture to compare the position of the CL peak with the calculated bandgaps. We consider the CL peak at 2.25eV for the comparison. The triclinic ($P\underline{1}$) symmetry of $CsPb(I_{0.9}Br_{0.1})_3$ with a bandgap of 2.26eV is the closest to the CL peak followed by the tetragonal ($P4mm$) and the ordered orthorhombic ($Pnma$) symmetries with a bandgap of 2.15 and 2.18 eV, respectively. Conversely, the indexing of electron diffraction patterns showed a better match with the ordered orthorhombic symmetry than with the triclinic and tetragonal ones. We thus propose that the $CsPb(I_{0.9}Br_{0.1})_3$ phase crystallized in the orthorhombic ordered crystal system ($Pnma$).

Table 2 – Calculated lattice parameters (a, b and c in Å, and angles in °) and band gaps (in eV) for the different compounds identified in this work. A selection of experimental data are given for comparison. The references: a[51]; b[52]; c[53]; d [54]; e[55]; f[56]; g[57]; h [58]

Compounds	Space group	Lattice parameters			Band gaps	
			Calc	Exp.	Calc.	Exp.
$CsPbI_3$	$Pm\underline{3}m$	a	6.196	6.189[a], 6.198[b]	1.61	1.73[a], 1.76[c]
$CsPb(I_{0.93}Br_{0.07})_3$	$Pm\underline{3}m$	a	6.192		2.06	
	$P4mm$	a c	6.176 6.124		2.15	
	$P\underline{1}$	a b c α β γ	6.134 6.099 6.110 87.93 90.80 89.47		2.26	
	$Pnma$ *ord.*	a b c	9.055 12.395 8.052		2.18	
	$Pnma$ *disord.*	a b c	10.207 4.744 17.620		3.49	
$CsPbBr_3$	$Pm\underline{3}m$	a	5,884	5.883[b], 5.870[g]	2.20	2.25[d], 2.30[e]
$CsPb_2I_5$	$I4/mcm$	a c	8.914 15.567	9.060[f] 15.901[f]	2.83	2.40[f]
$CsPb_2(I_{0.7}Br_{0.3})_5$	$P4/m$	a c	8.768 15.525		2.99	

$CsPb_2Br_5$	$I4/mcm$	a	8.417	8.450[g], 8.483[h]	3.98	3.87[g]
		c	15.479	15.070[g], 15.250[h]		

We then performed cryogenic CL measurements to analyze the evolution of optoelectronics properties as the temperature of the sample decreases. **Figure S7(b)** shows the spatially averaged CL spectra normalized for various temperatures ranging from 300 down to 30K. The evolution of the position, the intensity, and the linewidth (FWHM) of the CL peak at 2.25eV are plotted as a function of temperature (see **Figure S7(c)**).

As the temperature decreases, the CL peak intensity increases, suggesting that the associated radiative recombination process is facilitated at lower temperatures. This evolution may be attributed to the suppression of non-radiative recombination processes that quenched the emission at ambient temperature [59]. Then, the FWHM of the CL peak decreases with decreasing temperature, which may be due to the reduced interactions between the generated carriers and phonons [60]. Finally, the position of the CL peak exhibits a non-monotonic evolution between 2.15 and 2.25eV. This evolution of the emission may result from the interplay of the contributions from thermal lattice shrinkage, which induces a shrinkage of the bandgap, and phase transitions, that occur with decreasing temperature [61].

A similar characterization protocol is carried out on the $CsPb_2(I_{0.7}Br_{0.3})_5$ needle displayed in **Figure 4(b)**. **Figure 4(e)** shows the electron diffraction pattern obtained on the FIB-milled lamella specimen displayed in **Figure S5(b)**. As for the first needle, this electron diffraction pattern is composed of spots indicating that the second needle consists of a single monocrystal. The tetragonal ($P4/m$) structures of $CsPb_2(I_{0.7}Br_{0.3})_5$, ($I4/mmc$) $CsPb_2I_5$, and $CsPb_2Br_5$ have been simulated by DFT. The obtained lattice parameters and bandgaps are shown in **Table 2**. The simulation of electron diffraction patterns from these phases is compared to the experimental diffraction pattern in **Figure S6.B**. The tetragonal $CsPb_2(I_{0.7}Br_{0.3})_5$ matches well the experimental data with less than 0.51 mm² Σs^2 error. The needle tetragonality is further supported by the emergence of a similar phase in the XRD diffraction pattern shown in **Figure 1(c)**. We can therefore ascribe the appearance of the tetragonal phase in CsMAFA perovskite aged to the formation of such needles. Microscopic investigation of the aged films strengthens results obtained via macroscopic measurements.

Figure 4(h) shows the spatially averaged CL spectrum in the blue-dashed square displayed on the SEM image **Figure 4(e)**. Three CL peaks are present: a broadband peak around 1.70eV, a narrow green emission peak at 2.45eV, and a low-intensity peak around 2.71eV. **Figure S8** presents CL maps filtered on the following spectral ranges:1.6±0.01eV, 2.41±0.05eV, and

2.71±0.09eV. Regardless of the filtered CL map, the needle does not emit, which suggests that none of the CL peaks mentioned can be related to the degradation product itself. The CL peaks at 1.70 and 2.45eV are mainly due to small particles, which can be attributed to residual CsMAFA perovskite (that did not fully decompose during aging) and PbI_2 clusters, respectively (see **Figure S8)**. As previously observed, the CL peak positioned at 2.71eV originates from the FTO beneath the needle. These observations show that the two needles considered exhibit very distinct optoelectronic property further supporting the assumption of distinct phases.

The CL spectrum **Figure 4(h)** is fitted with three Gaussian functions and a relatively large offset representing the background signal. The latter is significant due to the overall low intensity of the CL spectrum.

The correlation between XRD, EDS, and SAED results leads us to speculate the formation of $CsPb_2(I_{0.7}Br_{0.3})_5$. However, we do not observe any specific optical emission originating from this phase, and it is worth noting that the luminescence of $CsPb_2Br_5$ is still under debate in the literature [62].

The optical properties of this specimen have been further investigated with cryo-CL measurements. The spatially averaged CL spectra at 300, 200 and 150K are displayed in **Figure S8(b)**. The intensity of PbI_2 and CsMAFA perovskite CL peak (at 2.45 and 1.71eV) increases as the temperature decreases as expected. Notably, the CL signal below 1.5eV increases as well suggesting the presence of an emission peak at lower energy.

Motivated by this observation, we performed new CL acquisitions between 1.2 and 1.8eV. The measurements were conducted on another needle-like structure showing the same CL signal at room temperature (see SEM image in **Figure S9(a)**). The CL spectra at 200, 150, 100, 70, and 35K are displayed in **Figure S9(b)**. Three CL peaks are present and their intensities increase as temperature decreases. They are positioned at 1.6, 1.55, and 1.3eV. The former two might be related to the remaining CsMAFA perovskite, while the latter, which is rather broad even at low temperature, must originate from the needle. If we assume that this broad peak originates from band-to-band recombination, its energy suggests that the needle bandgap is close to 1.30eV.

This observation contradicts with the bandgap calculated for the tetragonal $CsPb_2(I_{0.7}Br_{0.3})_5$ phases at 2.99eV[63]. The results of our calculations, displayed in **Table 2**, indicate that the $CsPb_2Br_5$ exhibits an indirect bandgap of up to 3.98eV (found at experimentally at 3.87eV [57]). However, several experimental studies have reported absorption and emission spectra (obtained by UV-vis and PL spectroscopy) with an optical transition at 2.35eV [38,40] which conflicts with this theoretical bandgap. The same discrepancy is observed for the $CsPb_2I_5$ phase, for which we

estimated the bandgap at 2.83eV (found experimentally at 2.40eV [56]) while PL peaks were observed at 1.77eV in the literature [64].

Our theoretical and experimental bandgaps found in the literature are in quite good agreement, which is not consistent with our observations. However, we expected from $CsPb_2(I_{0.7}Br_{0.3})_5$ a CL emission peak at higher energy than the PL emission peak of the pure $CsPb_2I_5$. Further experimental analysis would be required to fully understand this discrepancy.

The CL peak position is constant regardless of the temperature of acquisition and the shape of the peak is broad suggesting a deep defect-mediated recombination process as in $CsPb(I_{0.9}Br_{0.1})_3$ needle [61]. The origin of this CL peak remains unclear but these results still provide material for the study of the luminescence of these cesium-based materials, which are currently widely investigated [65,66].

In the **Figure 1(b)**, we highlighted the emergence of other degradation features referred to as 'discs' and 'flowers'. The same analysis has been carried out on these degradation products and the results are presented in **Figure S10** and **S11** along with explanations details. The discs exhibit PbI_2 hexagons surrounded by perovskite film showing bigger grains and an enhanced red-shifted CL peak compared to the pristine perovskite. The latter observation indicates a variation of the composition reminding of localized iodine enrichment due to phase segregation. This feature might then be an intermediate state of the CsMAFA perovskite before its complete decomposition into PbI_2 under moisture exposure. Real-time observations and characterizations of the CsMAFA perovskite film during aging may help to directly link the dis and the formation of PbI_2 hexagons.

On the other hand, the investigation of a flower (see **Figure S10**) shows that it is composed of $CsPb_2(I_xBr_{1-x})_5$, similar to the second needle studied, with an I/Br ratio that varies depending on the region. These degradation products demonstrate the same optoelectronic response at room and low temperatures. Given the feature size and its peculiar shape, the flower might be the following stage of the second needle-like degradation product. Then again, clear observation of the needle 'blooming' into a 'flower' might be required to confirm this hypothesis.

In the light of these results, we now discuss the mechanisms involved in the formation of perovskite degradation products unveiled and outline possible pathways.

4. Discussion

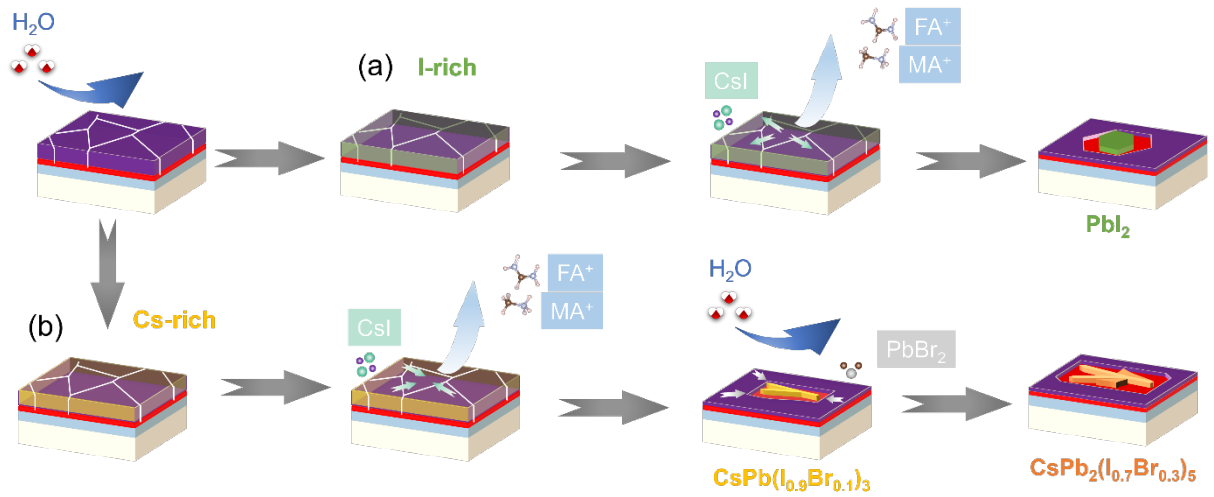

Figure 5 - Decomposition mechanisms proposed for the CsMAFA perovskite film under high relative humidity. Water molecules increase the mobility of ions, leading to the demixing of the CsMAFA film. Two distinct degradation mechanisms are proposed starting with this demixed film. (a) In the I-rich domains, organic cations and halides volatilize in the form of MAI ⍰ MA + HI (or FAI ⍰ FA + HI). Cs^+ cations migrate towards the surrounding film leaving behind PbI_2, forming hexagonal degradation products. (b) The same volatile species are extracted from the Cs-rich domains, leaving the remaining elements form $CsPb(I_{0.9}Br_{0.1})_3$ needles. Upon further moist air exposure, the latter grows into larger $CsPb_2(I_{0.7}Br_{0.3})_5$ needles by reacting with decomposition products, i.e., PbI_2 and $PbBr_2$, from surrounding material.

Our observations show that a CsMAFA film irreversibly transforms into various degradation products with distinct geometries upon exposure to high relative humidity levels. Based on our results, we propose degradation pathways of the CsMAFA perovskite film under moist air starting with a phase segregation. With increased humidity level, the ionic species become more mobile [17]. Halides migrate, which leads to the formation of I-rich and Br-rich regions in the film. The appearance of these regions is consistent with the red shift observed in PL emission in Section 2. A-site cations can also migrate, but at a much slower time scale, and their migration leads to Cs-rich, FA-rich, and MA-rich regions formation. Cation migration has been verified in mixed-cation perovskite film exposed to voltage bias, illumination, or heat [67–69]. Although no studies explicitly report that moisture favors cation migration, it increases the concentration of defects which promotes ion migration [67]. The unbalanced local concentration

in halides and cations leads to a complete demixing of purely inorganic and organic perovskites such as $CsPbX_3$ and $FA_{1-y}MA_yPbX_3$, respectively [70].

Prolonged humidity exposure enables organic A-site cations (FA^+ and MA^+) to volatilize following a redox reaction. According to Long et al., FA^+ cations have a stronger bond with Br^- than with I^- ions due to the larger electronegativityof Br^- ions [26]. They also showed that FA^+ cations volatilize preferentially with Br^- ions at temperatures above 250°C. In addition, Tan et al. have reported that CsMAFA perovskite films sequentially release MA^+ and FA^+ during annealing at 150°C in air with 60% RH [71]. We can then assume that our CsMAFA perovskite decomposition in humid air follows the same sequential pathway where MA^+ volatilize with I^-, followed by FA^+ with Br^-, and finally the remaining FA^+ with I^-, leaving Pb^{2+} and I^- to form hexagonal PbI_2 crystals. This process is summarized in the reaction displayed in **Equation S1** and schematically represented in **Figure 5(a)**.

The formation pathway of $CsPb(I_{0.9}Br_{0.1})_3$ initiated in Cs-rich regions of demixed CsMAFA perovskite is illustrated in **Figure 5(b)**. As described previously, it starts with the organic cations volatilizing with halides from the film exposed to humid air. However, depending on the composition of the segregated region in I and Cs, the number of reaction byproducts such as PbI_2 varies. Although in this study the exact quantities of byproducts could not be determined, we can still propose the reaction (1) as a hypothetic degradation pathway based on pristine CsMAFA perovskite.

$20*\mathbf{Cs_{0.05}(MA_{0.15}FA_{0.85})_{0.95}Pb(I_{0.84}\,Br_{0.16})_3}$ $H_2O \rightarrow \quad \mathbf{CsPb(I_{0.9}Br_{0.1})_3(s)} + 19*PbI_2(s) + 2.85*MAI(g) + 6.85*FAI(g) + 9.3*FABr(g)$	**(1)**

Notably, PbI_2 formation (reaction (S1)) could provide Cs^+ cations as reagents of the reaction (1), allowing the two to act together. Such concomitant reactions require a high diffusion coefficient of Cs^+ cations to allow their migration through the film. This coefficient is related to the activation energy barriers, which in turn depends on the material and its environmental conditions. Water molecules and oxygen are known to decrease such activation barriers through defect fabrication [17,72] and therefore Cs^+ cations could migrate sufficiently far in the film. A real-time observation of the formation of PbI_2 hexagons and the successive appearance of $CsPb(I_{0.9}Br_{0.1})_3$ needles could ultimately confirm our hypothesis.

Regarding $CsPb_2(I_{0.7}Br_{0.3})_5$, it has been shown in several publications [14,17,57,58,73] that $CsPbBr_3$ turns into $CsPb_2Br_5$ when exposed to moisture. According to Turedi et al. [14], this reaction occurs first through a complete decomposition of $CsPbBr_3$ into $PbBr_2$, Cs^+, and Br^-. The enrichment in $PbBr_2$ coupled with water molecules then gathers all the conditions to finally crystallize residual $CsPbBr_3$ in tetragonal $CsPb_2Br_5$. Conversely, Liu et al. claim that $CsPbBr_3$ transformation happens by losing CsBr through the action of water molecules [73]. Given these two mechanisms, we highly suspect that $CsPb(I_{0.9}Br_{0.1})_3$ needles transform into $CsPb_2(I_{0.7}Br_{0.3})_5$ needles during aging, as illustrated in **Figure 5(b)**. Their morphological similarity and the scarcity of $CsPb(I_{0.9}Br_{0.1})_3$ needles in aged film of more than 1 hour support this hypothesis. Drawing from the reasoning of Liu et al., we propose the hypothetical chemical reaction (2) where $CsPb(I_{0.9}Br_{0.1})_3$ loses Cs and I content, accompanied by PbI_2 formation. However, if we compare the size of the needles, we can see that $CsPb(I_{0.9}Br_{0.1})_3$ needles are smaller and thinner than $CsPb_2(I_{0.7}Br_{0.3})_5$ needles (see **Figures S1(a)** and **4**). It is then unlikely that losing material is the route followed during formation of the $CsPb_2(I_{0.7}Br_{0.3})_5$ needles.

$5*CsPb(I_{0.9}Br_{0.1})_3(s)\ H_2O \rightarrow CsPb_2(I_{0.7}Br_{0.3})_5(s) + 4*CsI(s) + 3*PbI_2(s)$	**(2)**

The chemical reaction (3a) presents the pathway proposed by Turedi et al. where the $CsPb_2(I_{0.7}Br_{0.3})_5$ needle forms by adding $PbBr_2$, and PbI_2 to a $CsPb(I_{0.9}Br_{0.1})_3$ needle. We assume that these are coming from the decomposition of pristine CsMAFA described in reaction (3b).

$CsPb(I_{0.9}Br_{0.1})_3(s) + 0.4*PbI_2(s) + 0.6PbBr_2(s)\ H_2O \rightarrow CsPb_2(I_{0.7}Br_{0.3})_5(s)$	**(3a)**
$2.5*Cs_{0.05}(MA_{0.15}FA_{0.85})_{0.95}Pb(I_{0.84}Br_{0.16})_3\ H_2O \rightarrow 0.4*PbI_2(s) + 0.6PbBr_2(s) + 1.5PbI_2(s) + 0.125*CsI(s) + 0.33625*MAI(g) + 2.01875*FAI(g)$	**(3b)**

This mechanism is the most plausible, considering the size of needles. The edges of the $CsPb(I_{0.9}Br_{0.1})_3$ needle in **Figure 4(a)** are positioned under the surrounding film which support the hypothesis that needles grow by consuming decomposition products of the surrounding film.

The emergence of different degradation products may lie in the compositional heterogeneity in the pristine thin film. In their recent contribution, Nishida et al. ascribe local preferential

degradations to cation inhomogeneities in the perovskite film. [33] Therefore, further measurements sensitive to these heterogeneities on the pristine film should be implemented in future studies.

The decrease of PbI_2 reflections in XRD diffractograms (see **Figure 1(d)**) coincides with the appearance of voids instead of PbI_2 hexagons after a few hours of aging (see **Figure S1(a)** at 120min), suggesting that PbI_2 is further decomposed. PbI_2 is known to decompose into metallic lead Pb^0 and I_2 with light [74] or lead salts such as PbO, $Pb(OH)_2$, or $PbCO_3$ in humid air[19]. Metallic Pb^0 is considered as a catalyst of hybrid perovskite decomposition. Therefore, degradation of hexagons might promote the overall decomposition of the thin film.
In addition, we observe that native PbI_2 clusters are absent in the surrounding of degradation products (see **Figure S1(b)**), indicating that they disappeared during the aging process. While describing the degradation product formation, the role of native PbI_2 clusters as reagents of the reaction was not considered. Lately, several published studies showed that clusters could dramatically affect perovskite integrity and, thus, solar cell stability [74–77]. Through decomposition, native PbI_2 clusters might be promoting the CsMAFA perovskite phase degradation. Consequently, further studies should also account for the effect of PbI_2 clusters on the parent perovskite film exposed to air with high relative humidity.

Conclusion

In this work, we investigated how triple-cation mixed-halide perovskite degrades when exposed to high relative humidity. The optoelectronic properties of the absorber evolve and the material forms different geometrical degradation features, which we analyzed systematically through correlation of CL, EDS, and SAED measurements. We have identified the chemical nature of these degradation features: PbI_2, $CsPbX_3$, and $CsPb_2X_5$, suggesting that degradation likely happens through different pathways.
The composition, the optical property, and the crystallographic orientation of the degradation features provide substantial knowledge of the degradation mechanisms. For PbI_2, microscopy shows that it grows along a preferential orientation (hexagonal [001] axis) which is corroborated by macroscopic XRD measurements. For $CsPb(I_{0.9}Br_{0.1})_3$, we showed that it most likely crystallizes in its orthorhombic ordered ($Pnma$) configuration. We also highlighted that the needle-like degradation features continue to evolve after their formation as they grow from $CsPbX_3$ to tetragonal ($P4/m$) $CsPb_2(I_{0.7}Br_{0.3})_5$.

Our results imply that oxygen combined with water molecules has several effects on CsMAFA: it helps ion migration, allows organic cations to escape from the material, and it enables recrystallization of remaining elements.

Conducting in-situ measurements is a major perspective of this work, as it enables to study the kinetics of degradation mechanisms under specific stress factors. Through these measurements, we could also confirm the hypothesized lineage between degradation products such as needles and "flowers". These measurements would provide insight into the early stages of CsMAFA degradation and strengthen our current understanding of the degradation mechanisms.

The coupling of multiple complementary electron microscopy techniques can be implemented on other compositions of hybrid halide perovskites. Understanding various degradation pathways could assist in the development of more stable hybrid perovskite devices and further enhances their photovoltaic performances.

Methodological Section

Materials :

FTO substrates were purchased from Solems. Titanium dioxide (TiO2) paste 30NR-D, methylammonium iodide (MAI, >99.99%), methylammonium bromide (MABr, >99.99%), formamidinium iodide (FAI, >99.99%), and FK 209 Co(III) TFSI salt were all purchased from Greatcell Solar Materials. Lead bromide (PbBr2, ultra dry 99.999%) and lead iodide (PbI2, ultra dry 99.999%) were purchased from Alfa Aesar. Cesium iodide (CsI, 99.999%), N,N-dimethylformamide (DMF, anhydrous 99.8%), dimethylsulfoxide (DMSO, ≥99.7%), chlorobenzene (CB, anhydrous 99.8%), isopropanol (IPA, anhydrous 99.5%), bis(trifluoromethane)sulfonimide lithium salt (Li-TFSI, 99.95%), and 4-tert-butylpyridine (t-BP, 98%) were all purchased from Sigma-Aldrich. 2,2′,7,7′-Tetrakis [N,N-di(4-methoxyphenyl)amino]-9,9′-spirobifluorene (Spiro-OMeTAD) was purchased from Borun New Materials. All materials were used without further purification

Half-devices fabrication :

FTO-coated glass substrates (2 × 2 cm2) were cleaned with sequential sonication in detergent (30 min), acetone (15 min), and isopropanol (15 min) baths at 50 °C. Following clear airflow drying, the cleaned substrates were treated with UV-ozone for 15 min. A compact-SnO2 electron transport layer (ETL) was made, thanks to chemical baths deposition. The glass/FTO/SnO2 substrates were treated with UV-Ozone for 30 min before being introduced in a glovebox for perovskite deposition.

The triple-cation perovskite solution was prepared by preparing a solution of CsI (1.5 mmol) in 1 mL of DMSO. This solution was stirred overnight at room temperature before being used. Another solution was prepared by dissolving MABr (0.2 mmol), PbBr2 (0.2 mmol), FAI (1 mmol), and PbI2 (1.1 mmol) in 1 mL of a DMF and DMSO mixture (4:1 volume ratio). After that, 1 mL of this solution was mixed with 42 μL of the CsI solution and stirred for another 15 min before deposition. To prepare 3D perovskite films, the perovskite solution was spin-coated on top of the TiO2 layer at 2000 rpm for 12 s. A second consecutive step of 30 s at 6000 rpm

was used to deposit 100 µL of CB, 12 s before the end of the rotation. The intermediate films were then annealed on a hot plate at 100 °C for 30 min for perovskite film formation.

Aging under controlled humidity procedure:

The aging set-up is drawn schematically described in **Figure 1(a)**. We cut a 2x2cm sample into four pieces, three are aged under specific conditions, and the last is used as reference. They are introduced in a chamber connected to a humidity controller (RH95 Linkam). To isolate the effect of the moisture, the chamber has been made opaque to light as illumination may interfere with the degradation mechanism. The system uses air as the carrier gas to transport (supply) vaporized water in the tank. As a result, the chamber atmosphere is maintained at a controlled relative humidity level, i.e., 85%. After different periods of time (one, two, and four hours), we take out a sample from the chamber and store it under a vacuum. Efforts are made to reduce the transfer time since it exposes the remaining samples to ambient illumination. Samples are then cut into smaller pieces to fit the various characterization machine holders.

This procedure eases characterizations as all samples from various degradation times are available at the end. However, it does not offer information on the reversible interactions between water and perovskite.

X-ray diffraction spectroscopy:

Measurements are performed using a Panalytical XRD analyzer (Cu Kα1α2 radiation, λ= 1.5418Å) with a scan range from 10 to 60° for 20 minutes. The obtained spectrum is normalized by its maximum. Since all specimens are not the same size, it is not relevant to compare their peak intensity. However, we can still interpret the ratio between peaks, i.e., crystallographic orientations.

Hyperspectral Photoluminescence (HI):

The hyperspectral imaging system records a luminescence intensity signal along three dimensions (x, y, λ). The set-up is composed by a home-built microscope with Thorlabs optomechanical elements, a 2D bandpass filtering system from company Photon Etc with 2 nm resolution, and a 1 Mpix silicon-based CCD camera PCO1300. The samples were illuminated

with a LED (λ= 405 nm) through an infinity-corrected ×10 Olympus objective with numerical aperture of 0.10, and the luminescence was collected through the same objective.
The excitation beam and luminescence signals were separated with appropriate Thorlabs dichroic beam splitter (DMLP650) and filters (FES 0450). The 2D luminescence signal was corrected for each pixel of the sensor from the spectral transmissions along all the optical path, from the read noise and dark current noise of the camera. All the acquisitions were performed in nitrogen atmosphere at the temperature of 20°C.

Scanning Electron Microscope (SEM) and Energy dispersive spectroscopy (EDS):
We use a Zeiss Merlin VP compact microscope to acquire SEM micrographs and EDS analysis. SEM is operated at an acceleration voltage of 3keV for imaging and 15keV for analytical study. An "in-lens" detector allows secondary (SE) and backscattered (BSE) electrons to be collected simultaneously. It enhances image resolution while providing topography and chemical information on the specimen. During EDS acquisition, we evaluate interaction depth as c.a. 1.2µm.

Cathodoluminescence (CL):
CL measurements are carried out in an Attolight Allalin 4027 Chronos quantitative CL microscope. We acquire CL maps at 6 keV acceleration voltage, implying a penetration depth c.a. 250 nm (calculated with CASINO simulation software), at 1 nA as beam current, at 20 ms dwell time, and with 128 rastering pixels. The field-of-view changes with the magnification ranging from 10 to 30 µm. Beam focusing is done before each map on sliver paste which fixes and connects the specimen electrically.

Scanning Transmission Electron Microscopy (STEM) EDS
Lamellae preparation was done with an field electron and ion company (FEI) Dual-Beam Helios. We used the FEI standard procedure for specimen thinning (which avoided most of ion-induced degradation). To investigate these specimens, a FEI Osiris transmission electron microscopy (TEM) was used in STEM mode. Acceleration voltage was kept at 200 kV and current < 500 pA during EDS and HAADF acquisition. Quantification of the elements was done using the Cliff-Lorimer method through the software Esprit 2 that has been previously calibrated for halides (iodine and bromine) determination with reference specimen.

Selected Area Diffraction

Same TEM is used to investigate the crystallinity of the lamellae prepared. In TEM mode the region-of-interest is selected and the microscope is adjusted. Then the selection area diaphragm of 10µm is introduced and the mode diffraction is selected. Diffractogram is acquired on a camera Gatan during less than 5s to hinder e-beam induced degradations.

Computational details:

The calculations have been performed with the periodic CRYSTAL code. [78–80] Within CRYSTAL, both the Hartree–Fock (HF) equations and the Kohn–Sham equations of the density functional theory (DFT), as well as hybrid schemes where the exchange operator is a linear combination of the HF and DFT ones, can be solved self-consistently. Basis sets suited for both pseudopotential and all-electron types of calculation, in the form of Gaussian-type functions (GTFs), can be used.

For this work, a hybrid exchange-correlation functional optimized to yield description of the structural, electronic, and dynamic properties of $CsPbX_3$ (X = Cl, Br and I) perovskites in good agreement with experiment, has been used [47]: the Hamiltonian combines 16% of HF exact exchange with the PBEsol exchange-correlation functional. [81] The used basis-sets for Cs, Pb and I are also described in Ref. [47].

For the evaluation of the Coulomb and exchange series within CRYSTAL, the truncation thresholds for the bielectronic integrals, as defined in the CRYSTAL manual [80], were set to 10^{-8}, 10^{-8}, 10^{-8}, 10^{-8}, and 10^{-16} a.u. The calculations have been performed with 14 × 14 × 14 Monkhorst–Pack *k*-point meshes [82] for the bulk materials, respectively. The convergence criteria on total energies (and for frequencies determination) were 10^{-9} (10^{-12}) Ha. Atomic displacements and forces thresholds were $1.8 \cdot 10^{-3}$ Bohr and $4.5 \cdot 10^{-4}$ Ha/Bohr, respectively. With these computational conditions, the obtained data can be considered as fully converged.

To obtain the atomic structure of the measured compositions for each type of perovskite in this work, a supercell approach was used:

(1) For each "commensurate" concentration, all nonidentical substitution patterns have been considered. For each of them, the lattice parameters and internal coordinates have been optimized, maintaining the symmetry imposed by composition in question.

(2) For the configuration minimizing the total energy, the calculation of Γ phonons was performed in order to verify the dynamic stability.

(3) In the case of the existence of unstable modes (those with imaginary frequency), the symmetry was correspondingly reduced and the structure optimization was redone to enable displacements corresponding to the phonon eigenvector of such an unstable mode.

(4) For each concentration, the most stable configuration was retained for subsequent structural optimization, followed by the calculation of vibrational frequencies (see the previous step) for the ultimate stability analysis. The phonon contribution (zero-point energy) was then taken into account for the ultimate assessment of the relative stability of configurations.

This method was used for determining the different phases subgroup of the cubic ($Pm\bar{3}m$) of $CsPb(I_{0.9}Br_{0.1})_3$; 7 different atomic configurations of a 135 atoms supercell corresponding to the obtained phases have been explored. Since the disordered and ordered Pnma phases of this compound is not a subgroup of the cubic phase, it was treated separately: a 180 atoms supercell was used in order to respect the Pnma symmetry and the composition; for the disordered and ordered phases 10 and 39 atomic configurations have been optimized.
For $CsPb_2(I_{0.7}Br_{0.3})_5$, to respect the composition, a 64 atoms supercell was used reducing the symmetry of the system from *I4/mcm* to *P4/m*, the described method was applied on this final system; in total 23 different atomic configurations have been probed. **Table 2** summarizes the obtained final atomic structure for each composition and symmetry of each perovskites studied in this work.

Supporting Information
Supporting Information is available from the Wiley Online Library or from the author.

Acknowledgements

The authors thank the ANRT (French National Association for Research and Technology) for its financial support within CIFRE agreement 2019/0948 (industrial convention for training through research). This work was also supported by the French government in the framework of the program of investments for the future (Programme d'Investissement d'Avenir ANR-IEED-002-01).

References

[1] D. W. de Quilettes, S. M. Vorpahl, S. D. Stranks, H. Nagaoka, G. E. Eperon, M. E. Ziffer, H. J. Snaith, D. S. Ginger, *Science* **2015**, *348*, 683.
[2] Q. Dong, Y. Fang, Y. Shao, P. Mulligan, J. Qiu, L. Cao, J. Huang, *Science* **2015**, *347*, 967.
[3] S. D. Stranks, G. E. Eperon, G. Grancini, C. Menelaou, M. J. P. Alcocer, T. Leijtens, L. M. Herz, A. Petrozza, H. J. Snaith, *Science* **2013**, *342*, 341.
[4] C. C. Boyd, R. Cheacharoen, T. Leijtens, M. D. McGehee, *Chem. Rev.* **2019**, *119*, 3418.
[5] J.-P. Correa-Baena, M. Saliba, T. Buonassisi, M. Grätzel, A. Abate, W. Tress, A. Hagfeldt, *Science* **2017**, *358*, 739.
[6] R. Wang, M. Mujahid, Y. Duan, Z. Wang, J. Xue, Y. Yang, *Adv. Funct. Mater.* **2019**, *29*, 1808843.

[7] C. Yang, R. Zhi, M. U. Rothmann, F. Huang, Y.-B. Cheng, W. Li, *Solar RRL* **2022**, *6*, 2100600.
[8] L. Fan, Z. Pei, P. Wang, Z. Zheng, *J. Electron. Mater.* **2022**, *51*, 2801.
[9] J. Hidalgo, C. A. R. Perini, A.-F. Castro-Mendez, D. Jones, H. Köbler, B. Lai, R. Li, S. Sun, A. Abate, J.-P. Correa-Baena, *ACS Energy Lett.* **2020**, *5*, 3526.
[10] E. J. Juarez-Perez, M. Haro, *Science* **2020**, *368*, 1309.
[11] M. V. Khenkin, E. A. Katz, A. Abate, G. Bardizza, J. J. Berry, C. Brabec, F. Brunetti, V. Bulović, Q. Burlingame, A. Di Carlo, R. Cheacharoen, Y.-B. Cheng, A. Colsmann, S. Cros, K. Domanski, M. Dusza, C. J. Fell, S. R. Forrest, Y. Galagan, D. Di Girolamo, M. Grätzel, A. Hagfeldt, E. von Hauff, H. Hoppe, J. Kettle, H. Köbler, M. S. Leite, S. Liu, Y.-L. Loo, J. M. Luther, C.-Q. Ma, M. Madsen, M. Manceau, M. Matheron, M. McGehee, R. Meitzner, M. K. Nazeeruddin, A. F. Nogueira, Ç. Odabaşı, A. Osherov, N.-G. Park, M. O. Reese, F. De Rossi, M. Saliba, U. S. Schubert, H. J. Snaith, S. D. Stranks, W. Tress, P. A. Troshin, V. Turkovic, S. Veenstra, I. Visoly-Fisher, A. Walsh, T. Watson, H. Xie, R. Yıldırım, S. M. Zakeeruddin, K. Zhu, M. Lira-Cantu, *Nat Energy* **2020**, *5*, 35.
[12] Y. An, J. Hidalgo, C. A. R. Perini, A.-F. Castro-Méndez, J. N. Vagott, K. Bairley, S. Wang, X. Li, J.-P. Correa-Baena, *ACS Energy Lett.* **2021**, *6*, 1942.
[13] Z. Chen, G. Brocks, S. Tao, P. A. Bobbert, *Nature Communications* **2021**, *12*, 2687.
[14] B. Turedi, K. J. Lee, I. Dursun, B. Alamer, Z. Wu, E. Alarousu, O. F. Mohammed, N. Cho, O. M. Bakr, *J. Phys. Chem. C* **2018**, *122*, 14128.
[15] H.-J. Lin, S. Cacovitch, A. Rebai, J. Rousset, C. Longeaud, *ACS Appl. Mater. Interfaces* **2020**, acsami.0c01732.
[16] J. M. Howard, E. M. Tennyson, S. Barik, R. Szostak, E. Waks, M. F. Toney, A. F. Nogueira, B. R. A. Neves, M. S. Leite, *J. Phys. Chem. Lett.* **2018**, *9*, 3463.
[17] D. Di Girolamo, M. I. Dar, D. Dini, L. Gontrani, R. Caminiti, A. Mattoni, M. Graetzel, S. Meloni, *J. Mater. Chem. A* **2019**, *7*, 12292.
[18] Y. Lu, Z. Si, H. Liu, Y. Ge, J. Hu, Z. Zhang, X. Mu, K. Selvakumar, M. Sui, *Chem. Eur. J.* **2021**, *27*, 3729.
[19] P. E. Marchezi, E. M. Therézio, R. Szostak, H. C. Loureiro, K. Bruening, A. Gold-Parker, M. A. Melo, C. J. Tassone, H. C. N. Tolentino, M. F. Toney, A. F. Nogueira, *J. Mater. Chem. A* **2020**, *8*, 9302.
[20] E. J. Juarez-Perez, L. K. Ono, M. Maeda, Y. Jiang, Z. Hawash, Y. Qi, *J. Mater. Chem. A* **2018**, *6*, 9604.
[21] Z. Fan, H. Xiao, Y. Wang, Z. Zhao, Z. Lin, H.-C. Cheng, S.-J. Lee, G. Wang, Z. Feng, W. A. Goddard, Y. Huang, X. Duan, *Joule* **2017**, *1*, 548.
[22] E. J. Juarez-Perez, L. K. Ono, Y. Qi, *J. Mater. Chem. A* **2019**, *7*, 16912.
[23] E. Smecca, Y. Numata, I. Deretzis, G. Pellegrino, S. Boninelli, T. Miyasaka, A. L. Magna, A. Alberti, *Physical Chemistry Chemical Physics* **2016**, *18*, 13413.
[24] M. A. Akhavan Kazemi, P. Raval, K. Cherednichekno, J. Chotard, A. Krishna, A. Demortiere, G. N. M. Reddy, F. Sauvage, *Small Methods* **2021**, *5*, 2000834.
[25] K. Ho, M. Wei, E. H. Sargent, G. C. Walker, *ACS Energy Lett.* **2021**, *6*, 934.
[26] M. Long, T. Zhang, M. Liu, Z. Chen, C. Wang, W. Xie, F. Xie, J. Chen, G. Li, J. Xu, *Advanced Materials* **2018**, *30*, 1801562.
[27] Y. Hu, M. F. Aygüler, M. L. Petrus, T. Bein, P. Docampo, *ACS Energy Lett.* **2017**, *2*, 2212.
[28] M. A. A. Kazemi, N. Folastre, P. Raval, M. Sliwa, J. M. V. Nsanzimana, S. Golonu, A. Demortiere, J. Rousset, O. Lafon, L. Delevoye, others, *Energy & Environmental Materials* **2023**, *6*, e12335.
[29] T. A. S. Doherty, S. Nagane, D. J. Kubicki, Y.-K. Jung, D. N. Johnstone, A. N. Iqbal, D. Guo, K. Frohna, M. Danaie, E. M. Tennyson, S. Macpherson, A. Abfalterer, M. Anaya, Y.-H. Chiang, P. Crout, F. S. Ruggeri, S. Collins, C. P. Grey, A. Walsh, P. A. Midgley, S. D. Stranks, *Science* **2021**, *374*, 1598.

[30] S. Macpherson, T. A. S. Doherty, A. J. Winchester, S. Kosar, D. N. Johnstone, Y.-H. Chiang, K. Galkowski, M. Anaya, K. Frohna, A. N. Iqbal, S. Nagane, B. Roose, Z. Andaji-Garmaroudi, K. W. P. Orr, J. E. Parker, P. A. Midgley, K. M. Dani, S. D. Stranks, *Nature* **2022**, *607*, 294.
[31] J. Llacer, D. Moerman, O. Douhéret, X. Noirfalise, C. Quarti, R. Lazzaroni, D. Théron, P. Leclère, *ACS Appl. Nano Mater.* **2020**, *3*, 8268.
[32] T. Hwang, A. J. Yun, B. Lee, J. Kim, Y. Lee, B. Park, *Journal of Applied Physics* **2019**, *126*, 023101.
[33] J. Nishida, A. H. Alfaifi, T. P. Gray, S. E. Shaheen, M. B. Raschke, *ACS Energy Lett.* **2020**, *5*, 1636.
[34] F. Hao, C. C. Stoumpos, Z. Liu, R. P. H. Chang, M. G. Kanatzidis, *J. Am. Chem. Soc.* **2014**, *136*, 16411.
[35] B. Roose, K. Dey, Y.-H. Chiang, R. H. Friend, S. D. Stranks, *J. Phys. Chem. Lett.* **2020**, *11*, 6505.
[36] X. Tang, Z. Hu, W. Yuan, W. Hu, H. Shao, D. Han, J. Zheng, J. Hao, Z. Zang, J. Du, Y. Leng, L. Fang, M. Zhou, *Advanced Optical Materials* **2017**, *5*, 1600788.
[37] I. Dursun, M. De Bastiani, B. Turedi, B. Alamer, A. Shkurenko, J. Yin, A. M. El-Zohry, I. Gereige, A. AlSaggaf, O. F. Mohammed, M. Eddaoudi, O. M. Bakr, *ChemSusChem* **2017**, *10*, 3746.
[38] J. A. Christians, P. A. Miranda Herrera, P. V. Kamat, *J. Am. Chem. Soc.* **2015**, *137*, 1530.
[39] M. A. A. Kazemi, N. Folastre, P. Raval, M. Sliwa, J. M. V. Nsanzimana, S. Golonu, A. Demortiere, J. Rousset, O. Lafon, L. Delevoye, G. N. M. Reddy, F. Sauvage, *ENERGY & ENVIRONMENTAL MATERIALS n/a*.
[40] S. Svanström, T. J. Jacobsson, G. Boschloo, E. M. J. Johansson, H. Rensmo, U. B. Cappel, *ACS Appl. Mater. Interfaces* **2020**, *12*, 7212.
[41] A. Delamarre, L. Lombez, J.-F. Guillemoles, *Applied Physics Letters* **2012**, *100*, 131108.
[42] Z. Song, N. Shrestha, S. C. Watthage, G. K. Liyanage, Z. S. Almutawah, R. H. Ahangharnejhad, A. B. Phillips, R. J. Ellingson, M. J. Heben, *J. Phys. Chem. Lett.* **2018**, *9*, 6312.
[43] E. T. Hoke, D. J. Slotcavage, E. R. Dohner, A. R. Bowring, H. I. Karunadasa, M. D. McGehee, *Chem. Sci.* **2015**, *6*, 613.
[44] P. Caprioglio, S. Caicedo-Dávila, T. C.-J. Yang, C. M. Wolff, F. Peña-Camargo, P. Fiala, B. Rech, C. Ballif, D. Abou-Ras, M. Stolterfoht, S. Albrecht, Q. Jeangros, D. Neher, *ACS Energy Lett.* **2021**, 419.
[45] S. Cacovich, D. Messou, A. Bercegol, S. Béchu, A. Yaiche, H. Shafique, J. Rousset, P. Schulz, M. Bouttemy, L. Lombez, *ACS Appl. Mater. Interfaces* **2020**, acsami.0c06844.
[46] D. B. Williams, C. B. Carter, *Transmission electron microscopy: a textbook for materials science*, 2nd ed., Springer, New York, **2008**.
[47] A. Mishra, P. Baranek, A. Postnikov, *Surfaces and Interfaces* **2021**, *25*, 101264.
[48] R. J. Sutton, M. R. Filip, A. A. Haghighirad, N. Sakai, B. Wenger, F. Giustino, H. J. Snaith, *ACS Energy Lett.* **2018**, *3*, 1787.
[49] R. E. Ferrell, G. G. Paulson, *Micron (1969)* **1977**, *8*, 47.
[50] E. Mugnaioli, G. Capitani, F. Nieto, M. Mellini, *American Mineralogist* **2009**, *94*, 793.
[51] A. Swarnkar, A. R. Marshall, E. M. Sanehira, B. D. Chernomordik, D. T. Moore, J. A. Christians, T. Chakrabarti, J. M. Luther, *Science* **2016**, *354*, 92.
[52] R. L. Moreira, A. Dias, *Journal of Physics and Chemistry of Solids* **2007**, *68*, 1617.
[53] M. Lai, Q. Kong, C. G. Bischak, Y. Yu, L. Dou, S. W. Eaton, N. S. Ginsberg, P. Yang, *Nano Res.* **2017**, *10*, 1107.
[54] M. Sebastian, J. A. Peters, C. C. Stoumpos, J. Im, S. S. Kostina, Z. Liu, M. G. Kanatzidis, A. J. Freeman, B. W. Wessels, *Phys. Rev. B* **2015**, *92*, 235210.

[55] J. Lin, M. Lai, L. Dou, C. S. Kley, H. Chen, F. Peng, J. Sun, D. Lu, S. A. Hawks, C. Xie, F. Cui, A. P. Alivisatos, D. T. Limmer, P. Yang, *Nature Materials* **2018**, *17*, 261.
[56] M. Li, S. Peng, S. Fang, Y. Gong, D. Yang, K. Bu, B. Liu, H. Luo, S. Guo, J. Li, H. Wang, Y. Liu, S. Jiang, C. Lin, X. Lü, *J. Phys. Chem. Lett.* **2022**, *13*, 2555.
[57] Z. Zhang, Y. Zhu, W. Wang, W. Zheng, R. Lin, F. Huang, *J. Mater. Chem. C* **2018**, *6*, 446.
[58] G. Li, H. Wang, Z. Zhu, Y. Chang, T. Zhang, Z. Song, Y. Jiang, *Chemical Communications* **2016**, *52*, 11296.
[59] J.-Y. Yang, M. Hu, *J. Phys. Chem. Lett.* **2017**, *8*, 3720.
[60] B. T. Diroll, H. Zhou, R. D. Schaller, *Advanced Functional Materials* **2018**, *28*, 1800945.
[61] H. C. Woo, J. W. Choi, J. Shin, S.-H. Chin, M. H. Ann, C.-L. Lee, *J. Phys. Chem. Lett.* **2018**, 9.
[62] P. Shen, X. Ma, F. Pan, Y. Wang, B. Liu, H. Ye, *J. Phys. Chem. C* **2021**, *125*, 6767.
[63] C. Qin, T. Matsushima, A. S. D. Sandanayaka, Y. Tsuchiya, C. Adachi, *J. Phys. Chem. Lett.* **2017**, *8*, 5415.
[64] K.-H. Wang, L. Wu, L. Li, H.-B. Yao, H.-S. Qian, S.-H. Yu, *Angewandte Chemie* **2016**, *128*, 8468.
[65] J. K. Nam, D. H. Chun, R. J. K. Rhee, J. H. Lee, J. H. Park, *Advanced Science* **2018**, *5*, 1800509.
[66] D. Yang, M. Cao, Q. Zhong, P. Li, X. Zhang, Q. Zhang, *J. Mater. Chem. C* **2019**, *7*, 757.
[67] L. Liu, J. Lu, H. Wang, Z. Cui, G. Giorgi, Y. Bai, Q. Chen, *Materials Reports: Energy* **2021**, *1*, 100064.
[68] N. Li, Y. Luo, Z. Chen, X. Niu, X. Zhang, J. Lu, R. Kumar, J. Jiang, H. Liu, X. Guo, B. Lai, G. Brocks, Q. Chen, S. Tao, D. P. Fenning, H. Zhou, *Joule* **2020**.
[69] I. M. Pavlovetc, M. C. Brennan, S. Draguta, A. Ruth, T. Moot, J. A. Christians, K. Aleshire, S. P. Harvey, S. Toso, S. U. Nanayakkara, J. Messinger, J. M. Luther, M. Kuno, *ACS Energy Lett.* **2020**, *5*, 2802.
[70] L. T. Schelhas, Z. Li, J. A. Christians, A. Goyal, P. Kairys, S. P. Harvey, D. Hoe Kim, K. H. Stone, J. M. Luther, K. Zhu, V. Stevanovic, J. J. Berry, *Energy & Environmental Science* **2019**, *12*, 1341.
[71] W. Tan, A. R. Bowring, A. C. Meng, M. D. McGehee, P. C. McIntyre, *ACS Appl. Mater. Interfaces* **2018**, *10*, 5485.
[72] S.-C. Liu, Z. Li, Y. Yang, X. Wang, Y.-X. Chen, D.-J. Xue, J.-S. Hu, *J. Am. Chem. Soc.* **2019**, *141*, 18075.
[73] M. Liu, J. Zhao, Z. Luo, Z. Sun, N. Pan, H. Ding, X. Wang, *Chem. Mater.* **2018**, *30*, 5846.
[74] J. Holovský, A. Peter Amalathas, L. Landová, B. Dzurňák, B. Conrad, M. Ledinský, Z. Hájková, O. Pop-Georgievski, J. Svoboda, T. C.-J. Yang, Q. Jeangros, *ACS Energy Lett.* **2019**, *4*, 3011.
[75] G. Tumen-Ulzii, C. Qin, D. Klotz, M. R. Leyden, P. Wang, M. Auffray, T. Fujihara, T. Matsushima, J.-W. Lee, S.-J. Lee, Y. Yang, C. Adachi, *Advanced Materials* **2020**, *32*, 1905035.
[76] H. Wang, Z. Wang, Z. Yang, Y. Xu, Y. Ding, L. Tan, C. Yi, Z. Zhang, K. Meng, G. Chen, Y. Zhao, Y. Luo, X. Zhang, A. Hagfeldt, J. Luo, *Advanced Materials* **2020**, *32*, 2000865.
[77] H. Zhang, W. Yu, J. Guo, C. Xu, Z. Ren, K. Liu, G. Yang, M. Qin, J. Huang, Z. Chen, Q. Liang, D. Shen, Z. Wu, Y. Zhang, H. T. Chandran, J. Hao, Y. Zhu, C. Lee, X. Lu, Z. Zheng, J. Huang, G. Li, *Advanced Energy Materials* **2022**, *12*, 2201663.
[78] R. Dovesi, A. Erba, R. Orlando, C. M. Zicovich-Wilson, B. Civalleri, L. Maschio, M. Rérat, S. Casassa, J. Baima, S. Salustro, B. Kirtman, *WIREs Computational Molecular Science* **2018**, *8*, e1360.
[79] A. Erba, J. Baima, I. Bush, R. Orlando, R. Dovesi, *J Chem Theory Comput* **2017**, *13*, 5019.
[80] R. Dovesi, F. Pascale, B. Civalleri, K. Doll, N. M. Harrison, I. Bush, P. D'Arco, Y. Noël, M. Rérat, P. Carbonnière, M. Causà, S. Salustro, V. Lacivita, B. Kirtman, A. M. Ferrari, F. S.

Gentile, J. Baima, M. Ferrero, R. Demichelis, M. De La Pierre, *J. Chem. Phys.* **2020**, *152*, 204111.
[81] J. P. Perdew, A. Ruzsinszky, G. I. Csonka, O. A. Vydrov, G. E. Scuseria, L. A. Constantin, X. Zhou, K. Burke, *Phys. Rev. Lett.* **2008**, *100*, 136406.
[82] H. J. Monkhorst, J. D. Pack, *Phys. Rev. B* **1976**, *13*, 5188.

Supporting Information

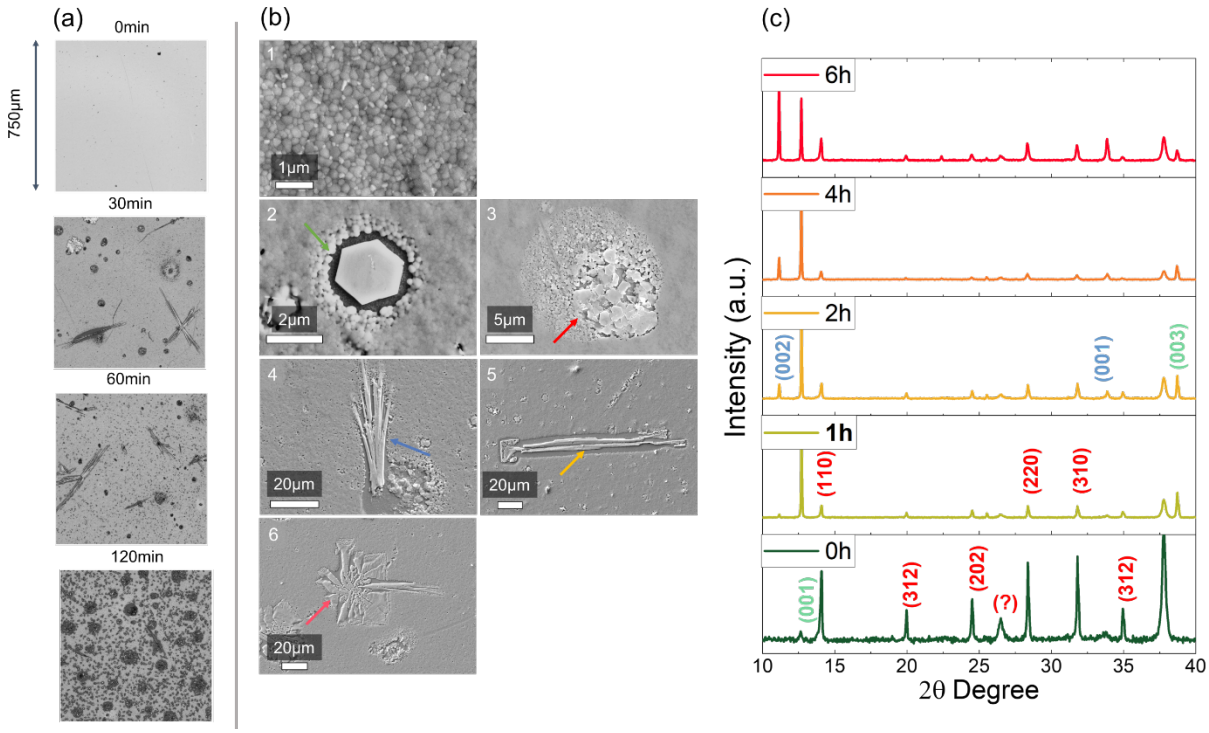

Figure S1. (a): Images of the pristine and the aged specimens were obtained with a confocal microscope. After only 30 minutes at 85% RH, degradation features appear in the film—same observations in the sample after 60 minutes. Sample aged 120 minutes shows more voids regions, hence less remnant perovskite film between degradation features. (b) SEM images corresponding to pristine sample (1), hexagon (2), disc (3), needles (4) and (5), and flower (6). Images are recorded with a secondary electron detector. (c) Serie of diffraction patterns obtained on specimen aged during 0,1,2 and 4 hours under 85% RH.

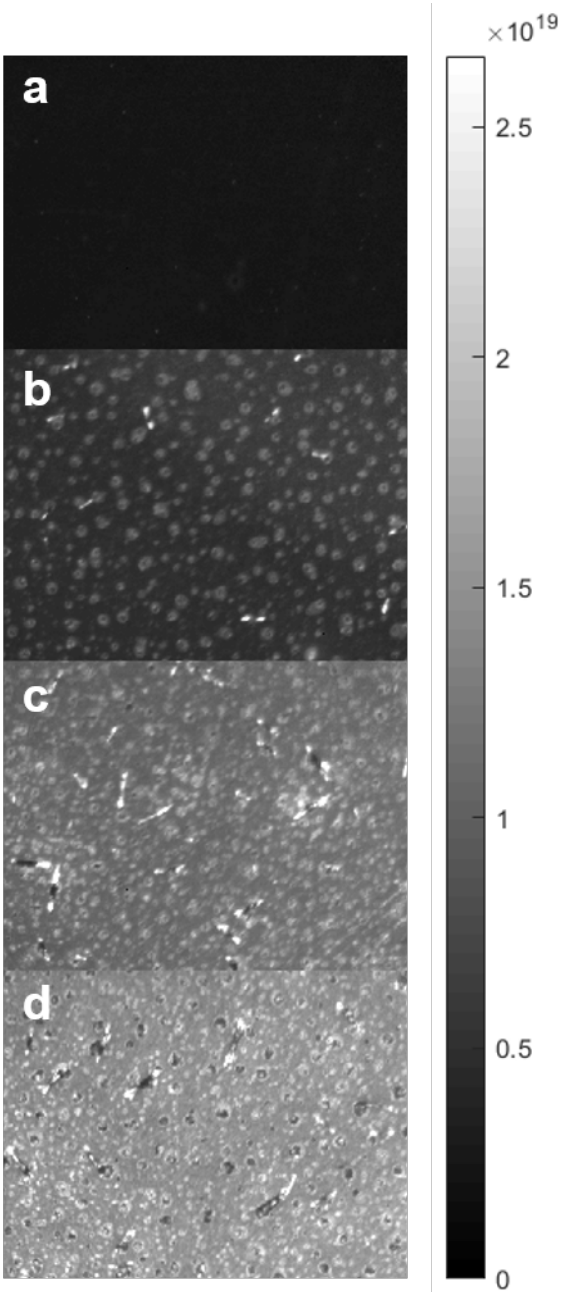

Figure S2. Panchromatic PL images of the perovskite films of a a) pristine samples and after b) 1hour, c) 2 hours, d) 4 hours of ageing time at 85% RH. The single image size is 750 μm x 900 μm.

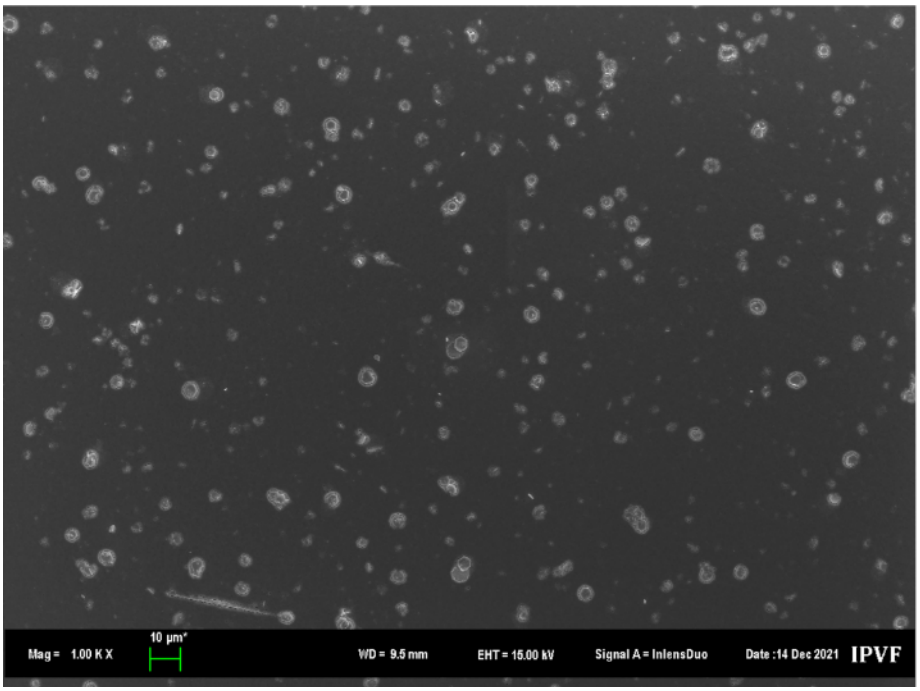

Grandeur	Value
% Total Area	10%
Mean size (µm)	10

Figure S3. SEM image of the specimen aged. This region exhibits mainly hexagons that are highly oriented. Using a watershed algorithm, we determined the % of the total area occupied by the hexagons and their averaged size.

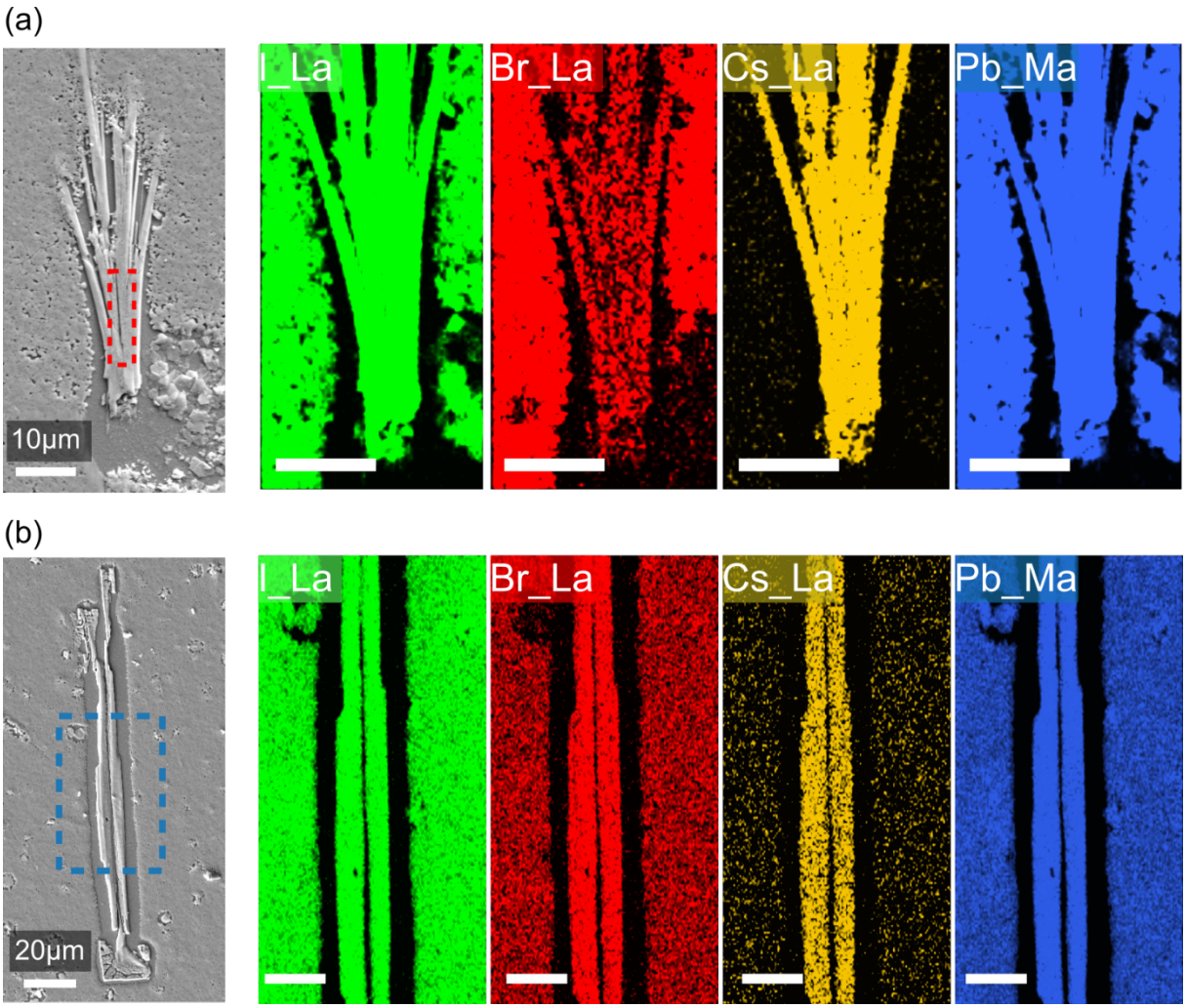

Figure S4. (a,b) SEM images of the two needles studied and corresponding SEM-EDS elemental maps (I, Br, Cs and Pb)..

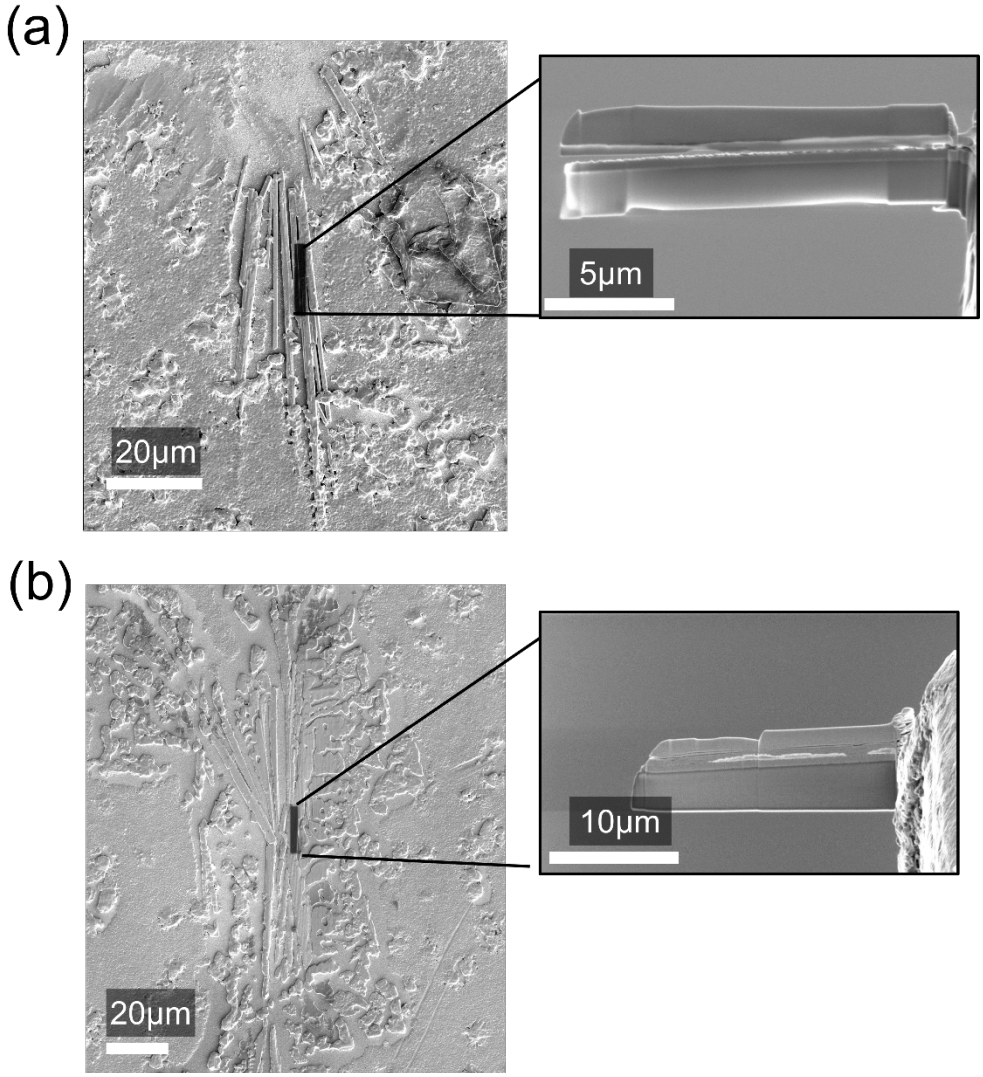

Figure S5. SEM image of the regions from which a FIB lamella has been extracted. Inset: SEM image of the lamella. (a) Needle $CsPb(I_{0.9}Br_{0.1})_3$ and (b) needle $CsPb_2(I_{0.7}Br_{0.3})_5$.

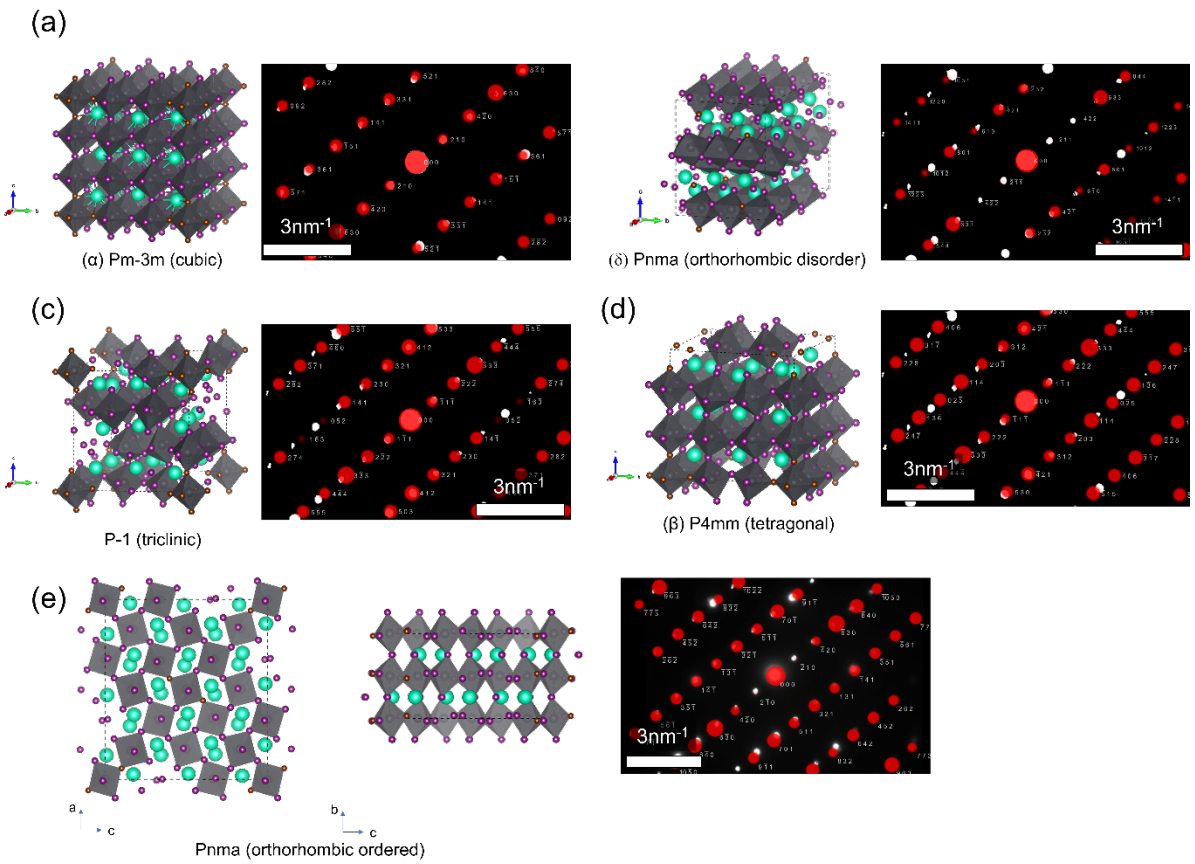

Figure S6.A – Indexation of the electron diffraction pattern from a $CsPb(I_{0.9}Br_{0.1})_3$ needle shown in **Figure 4(c)**. On the right: 'Balls and sticks' sketches of the simulated structures. On the left: Simulated electron diffraction patterns overlayed on experimental diffraction patterns.. **Table S1** summarizes for each crystal structure the zone axis matching better the experimental data and the sum-of-squares error (Σs^2) given by SingleCrystal software.

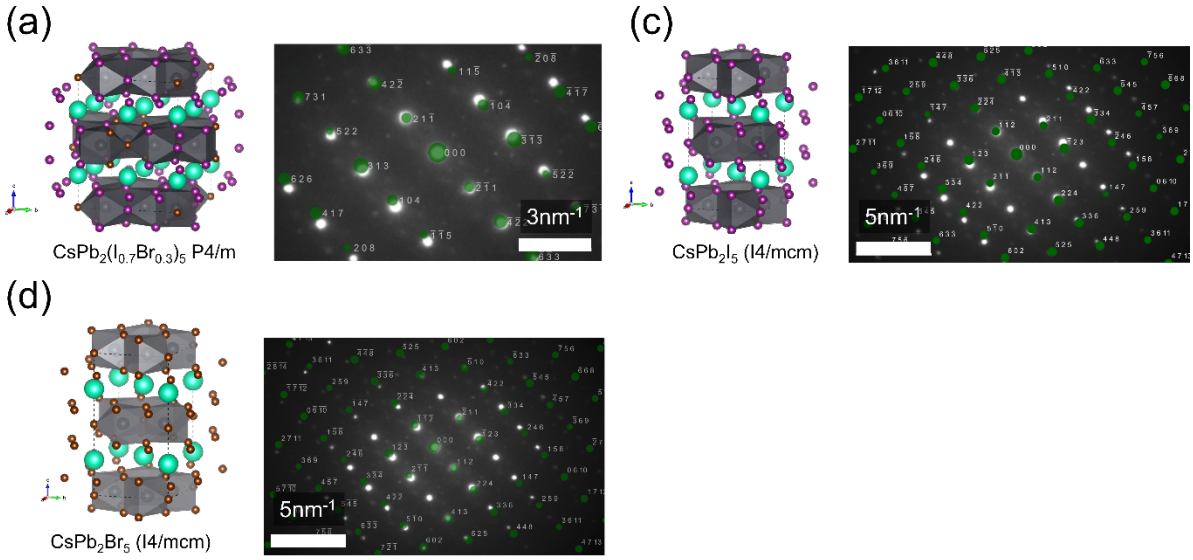

Figure S6.B – Indexation of the electron diffraction pattern from a $CsPb_2(I_{0.7}Br_{0.3})_5$ needle shown in **Figure 4(g).**

Table S1 - Details on the simulated electron diffraction patterns used to fit experimental diffraction patterns.

Phase	Crystal structure	Space group	RMS error (mm²)
$CsPb(I_{0.9}Br_{0.1})_3$	Cubic	$Pm\underline{3}m$	0.3
	Tetragonal	$P4mm$	1.54
	Triclinic	$P\underline{1}$	1.379
	Orthorhombic disordered	$Pnma$	0.77
	Orthorhombic ordered	$Pnma$	0.89
$CsPb_2I_5$	Tetragonal	$I4/mcm$	1.21
$CsPb_2(I_{0.7}Br_{0.3})_5$	Tetragonal	$P4/m$	0.371
$CsPb_2Br_5$	Tetragonal	$I4/mcm$	1.30

Table S2 - Fit parameters for **Figure 4(d)**

Emission peak (eV)	Intensity (cts/eV)	FWHM (eV)	Chemical formula
2.25	1.3e9	0.8	$CsPb(I_{0.9}Br_{0.1})_3$
1.65	1.1e9	0.1	CsMAFA
2.41	6.4e9	0.15	PbI_2
2.71	3.8e9	0.19	n/a

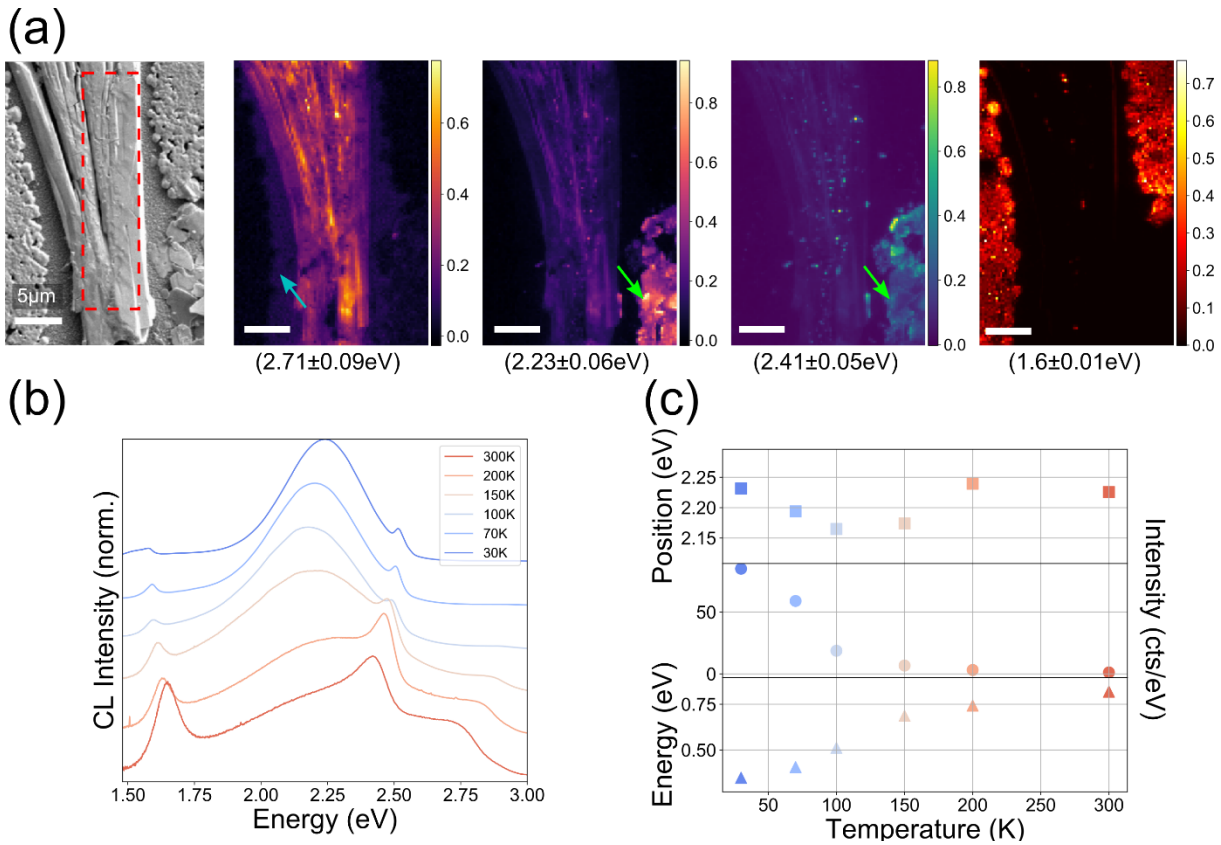

Figure S7. (a) SEM image of the $CsPb(I_{0.9}Br_{0.1})_3$ needle analyzed. CL maps with false colors showing the luminescence integrated over four different spectral regions: [2.62 eV, 2.8eV], [2.17 eV, 2.29 eV], [2.36 eV, 2.46 eV], and [1.59 eV, 1.61 eV]. The three latter corresponds to the emission of $CsPb(I_{0.9}Br_{0.1})_3$, the PbI_2 phase, and the CsMAFA perovskite respectively. For each pixel, the integrated intensity of each band is normalized by the maximum. (b) Spatially averaged CL spectra of the needle at 300, 200, 150, 100, 70, and 30 K. (c) The position, the intensity, and the FWHM of the emission peak position from $CsPb(I_{0.9}Br_{0.1})_3$ (2.25 eV at 300 K) as a function of temperature.

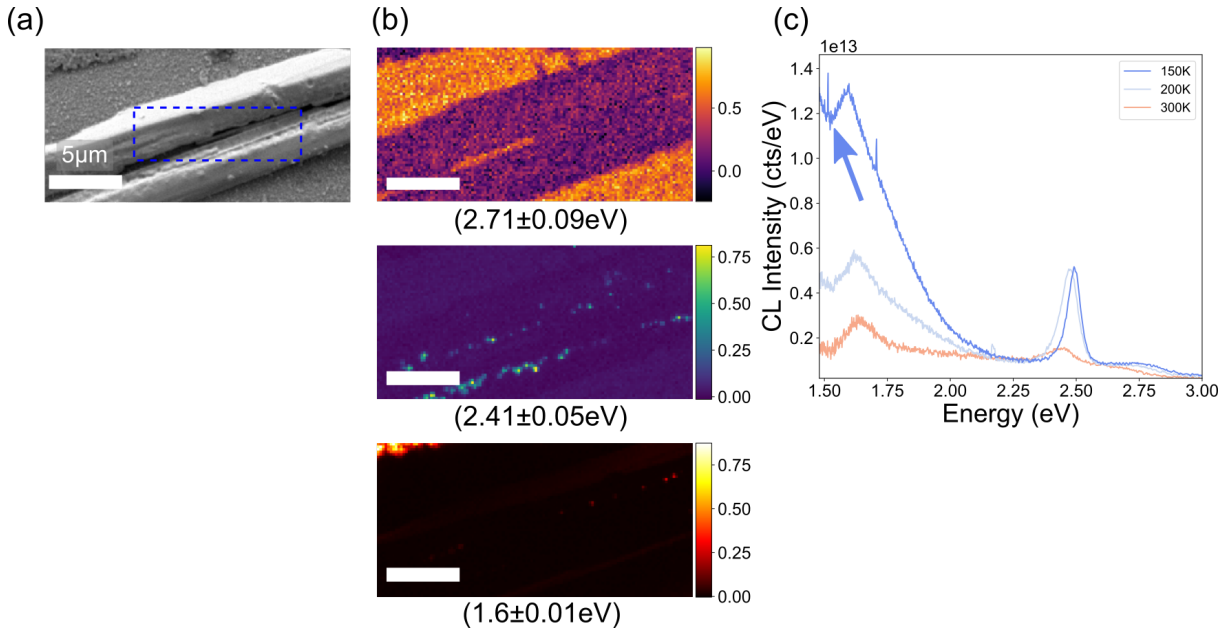

Figure S8. (a) SEM image of the analyzed $CsPb_2(I_{0.7}Br_{0.3})_5$ needle. (b) CL maps with false colors showing the luminescence integrated over three different spectral regions: [2.62 eV, 2.8 eV], [2.36 eV,2.46 eV], and [1.59 eV, 1.61 eV] corresponding to the emission of the FTO, the PbI_2, and the CsMAFA perovskite, respectively. For each pixel, the integrated intensity of each band is normalized by the maximum. (c) Spatially averaged CL spectra in the needle presented in (a) acquired at 300, 200, and 150 K.

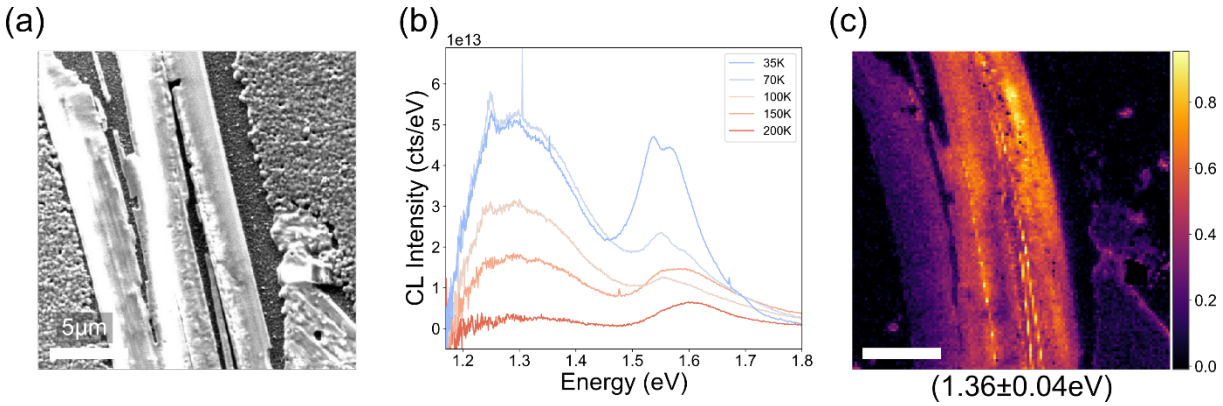

Figure S9. (a) SEM image of the analyzed $CsPb_2(I_{0.7}Br_{0.3})_5$ needle. (b) Spatially averaged CL spectra in the $CsPb_2(I_{0.7}Br_{0.3})_5$ needle presented in (a) at 200, 150, 100, 70, and 35 K. (c) CL map with false colors showing the luminescence integrated over the spectral region [1.32 eV, 1.4 eV] (normalized by the maximum integrated intensity in the map).

Equation S1 – Hypothetical chemical reaction leading to PbI_2 formation.

$Cs_{0.05}(MA_{0.15}FA_{0.85})_{0.95}Pb(I_{0.84}Br_{0.16})_3$ $H_2O \rightarrow PbI_2(s) + 0.1425*MAI(g) + 0.3775*FAI(g) + 0.43*FABr(g) + 0.05*CsBr(s)$	**(S1)**

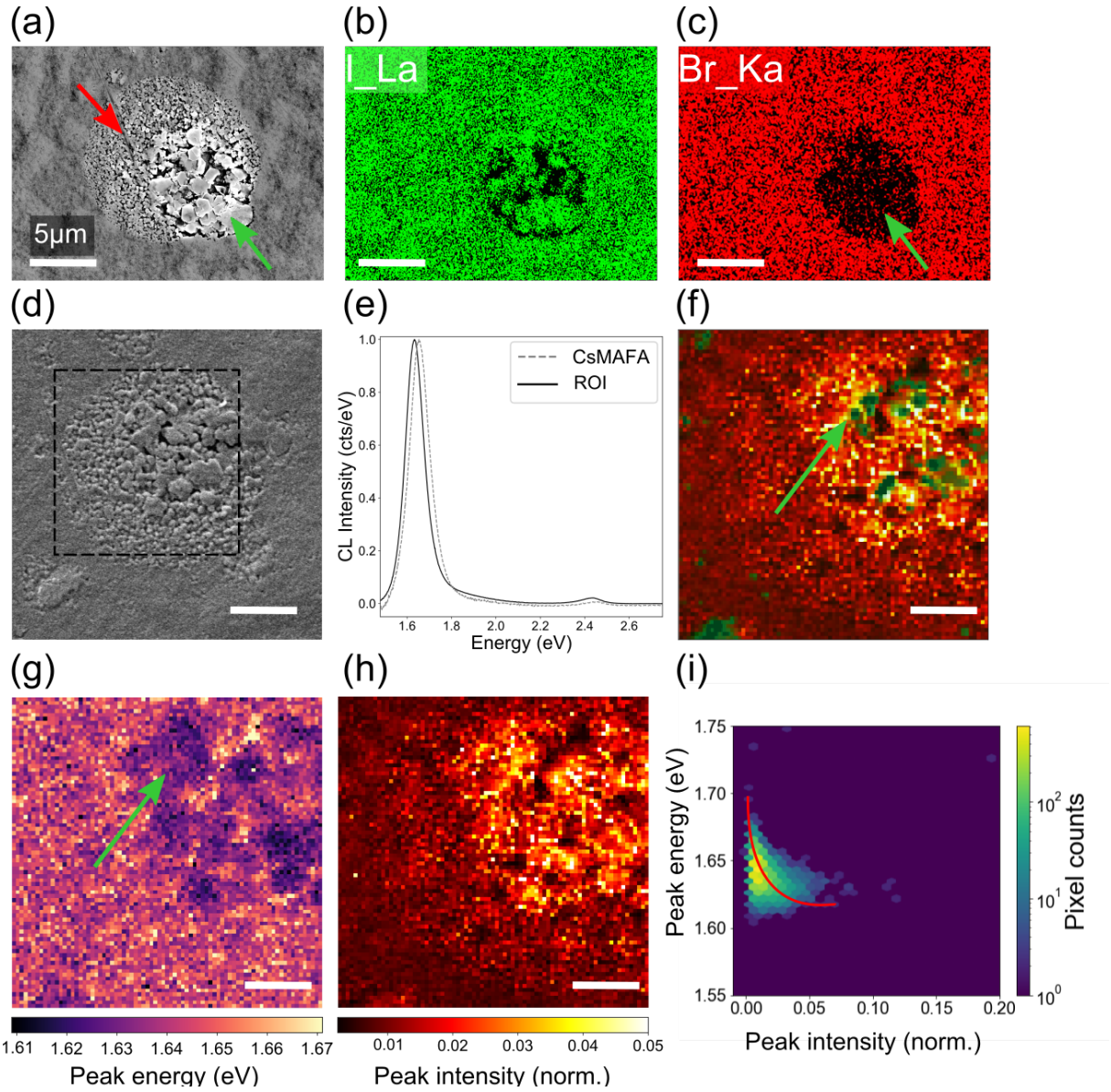

Figure S10. (a) SEM image of the disc-like degradation product analyzed with EDS. (b) and (c) Corresponding EDS elemental maps showing the distribution of iodine and bromine in green and red, respectively. (d) SEM image of the disc-like degradation product analyzed with CL. (e) CL spectra averaged over the region delimited by a black square on the SEM image, and in a pristine CsMAFA perovskite film, in black and gray (dash line), respectively. (f) CL map with false colors showing the luminescence integrated over two different spectral regions: red [1.6e V, 1.7 eV], and green [2.25 eV, 2.5 eV] corresponding to the emission of the CsMAFA perovskite and the PbI2 phase, respectively. For each pixel, the integrated intensity of each band is normalized by maximum. (g) CL peak energy (g) and intensity normalized map. (i) 2D histogram of the CL peak position as a function of its intensity normalized. The red line is a guide the eye.

Supplementary note : Disc-like degradation products

A similar analysis was performed on degradation products exhibiting a disc shape, as shown in **Figure 1(a)** and displayed at higher magnification in **Figure S1(b)(3)**. **Figure S10(a)** shows the SEM image of the feature analyzed with corresponding elemental maps of I and Br (in green and red respectively) distribution obtained by SEM-EDS.

The SEM image reveals three distinct regions: (1) micro-crystals indicated by a green arrow; (2) the film, near the micro-crystals, with large grains indicated by a red arrow; and (3) the surrounding bulk perovskite film. The composition in these three regions was estimated and is summarized in **Table S3**.

Table S3 – Results of the quantification of the composition in I, Br and Pb obtained via SEM-EDS measurements on three regions of the disc displayed in **Figure S10(a).**

Feature	I/Pb	Br/Pb
(1)	2.24±0.22	0.10±0.04
(2)	2.69±0.30	0.55±0.11
(3)	2.67±0.29	0.51±0.11

The elemental maps show that the micro-crystals have a higher I content and lower Br content compared to the surrounding regions. The estimated composition of these micro-crystals suggests that they are composed of PbI_2, similar to the hexagonal degradation products studied previously.

The area surrounding these PbI_2 crystals, which has larger grain size than the rest of the film, does not show any chemical variations in either elemental maps or the estimated composition. Previous studies have shown that hybrid perovskite crystallinity can be enhanced by humidity exposure. The emergence of the large-grain area in our samples may therefore be attributed to this phenomenon.

Figure S10(a) shows the SEM image of a similar degradation product analyzed using CL. The spatially averaged CL spectrum in the region delimited by the black square is plotted in black in **Figure S10(d)**. It exhibits a perovskite emission peak at 1.63 eV, slightly red-shifted (~20 meV) as compared to the reference spectrum shown in gray. A small contribution of the PbI_2 phase is also observed at 2.41 eV. A CL map with CsMAFA and PbI_2 peaks highlighted in red and green, respectively, is plotted in **Figure S10(f)**. This map shows the presence of PbI_2 micro-crystals, indicated by a green arrow, and reveals that the perovskite peak in the vicinity of these PbI_2 micro-crystals has a higher CL intensity than the rest of the film.

The position and intensity of the perovskite peak were then determined in the map and plotted in Figure S10(g) and (h). A local red-shift in the peak position is observed in the vicinity of the micro-crystals (indicated by a green arrow). The map Figure S10(h) suggests a correlation between this variation in peak position and the increase in peak intensity. This relationship is further supported by the 2D histogram displayed in Figure S10(i) (in which the peak position for all pixels in the map is on the ordinate, and the normalized intensity is on the abscissa). The trend line in red shows that the peak intensity evolves with the peak position for many pixel counts. This behavior can be attributed to the halide migration in a CsMAFA perovskite film,

which generates I-rich domains and causes similar variations in peak emission.

These observations suggest that exposure to moist air may induce halide segregation in the CsMAFA perovskite film followed by its decomposition into PbI_2 micro-crystals. Indeed, given the spatial proximity of the segregated phase of CsMAFA perovskite and the PbI_2 micro-crystals (see Figure S10(f) and (g)), we can hypothesize that halide segregation precedes the complete decomposition into PbI_2 crystals.

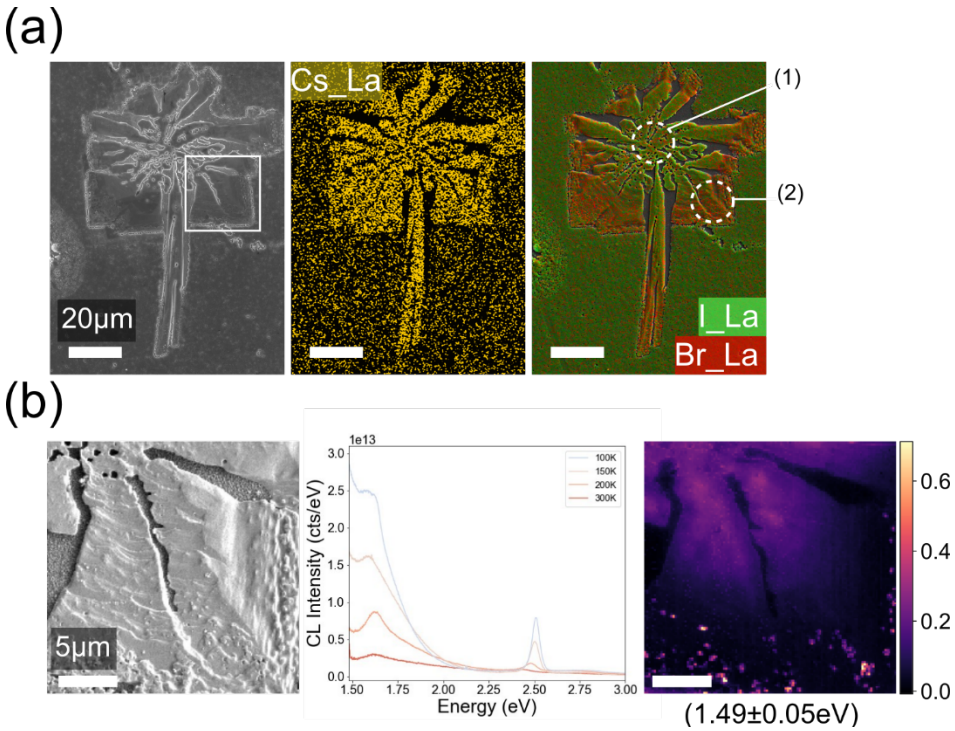

Figure S11-Flower feature : (a) SEM image of the flower analyzed and corresponding Cs elemental map obtained by SEM-EDS. On the right SEM image and corresponding Br and I elemental maps are overlayed. (b) SEM image of the region of the flower analyzed with CL and corresponding CL spectra acquired at 300, 200, 150, and 100K and a CL map with false colors showing the luminescence integrated over three the spectral region [1.44 eV, 1.54 eV].

Supplementary note : Analysis of the flower

The degradation product referred to as the "flower," shown in **Figures 1(a)** and **S1(b)(6)**, was then analyzed. **Figures S11(a)** and **(b)** display an SEM image of the degradation product along with Cs, I, and Br elemental maps obtained through SEM-EDS. I and Br maps are superimposed in the last image.

The Cs elemental map suggests that the flower has a higher Cs content compared to the surrounding perovskite film, similar to the observation made for the needles. In addition, the I/Br map indicates that the center of the flower has a higher I content than the edges, which are enriched in Br. The composition was estimated in two distinct regions indicated in the I/Br elemental map by circles. The results, summarized in **Table S4**, suggest that the flower is composed of $CsPb_2(I_xBr_{1-x})_5$, similar to the second needle studied, with an I/Br ratio that varies depending on the region probed.

Table S4 – Results of the quantification of the composition in Cs, I, Br and Pb obtained via SEM-EDS measurements on two regions of the flower displayed in **Figure S11(a).**

Feature	I/Pb	Br/Pb	Cs/Pb	Composition
(1)	2.11±0.24	0.60±0.11	0.57±0.10	$CsPb_2(I_{0.8}Br_{0.2})_5$
(2)	1.87±0.23	0.81±0.14	0.58±0.11	$CsPb_2(I_{0.7}Br_{0.3})_5$

CL was then performed in the area indicated in **Figure S11 (a)**. The SEM image of the area analyzed and filtered CL maps are presented in (c) and (d), respectively. The perovskite emission, shown in the first map, is localized in the edges of the degradation product in the form of small clusters. PbI_2, shown in the second map, is also localized in small clusters but is present throughout the flower. The third filter map shows that the center of the flower exhibits higher emission compared to the edges. This observation suggests that the I-rich regions are more prone to emit than the Br-rich regions.

The CL spectrum averaged over the degradation product has the same shape as that of the $CsPb_2(I_{0.7}Br_{0.3})_5$ needle (see **Figure S11(b)**). These degradation products demonstrate the same optoelectronic response at room temperature and low temperatures. Given the feature size and its peculiar shape, the flower might be the following stage of the second needle-like

degradation product. A direct observation of the needle "blooming" into a "flower" might be required to confirm this hypothesis.

Table S5 – Summary of the compositions, crystallographic and morphology of the various degradation products revealed in this study.

Compound	Morphology	Cs/Pb	I/Pb	Br/Pb	CL peak (nm)	XRD peak (2θ)
CsMAFA	Polycrystalline	0.07±0.02	2.5±0.3	0.5±0.1	760	14.09
PbI2	Hexagon (disc)	0±0	2.2±0.2	0.1±0.05	510	12.6
CsPb(I0.9Br0.1)3	Needle A	1.1±0.2	2.8±0.3	0.3±0.05	550	10
CsPb2(I0.7Br0.3)5	Needle B (flower)	0.6±0.1	2.0±0.2	0.7±0.1	740 and 930	11.2